Geomorphology 398 (2022) 108069

Contents lists available at ScienceDirect

Geomorphology

journal homepage: www.elsevier.com/locate/geomorph

Evolution and temporal constraints of a multiphase postglacial rock slope failure

Louise M. Vick *, Martin Mikkelsen [1], Geoffrey D. Corner, Sofia E. Kjellman, Leif Trønnes [2], Anne Hormes, Lis Allaart [3], Steffen G. Bergh

Department of Geosciences, UiT The Arctic University of Norway, Postbox 6050, Langnes, N-9037 Tromsø, Norway

ARTICLE INFO

Article history:
Received 26 June 2021
Received in revised form 1 December 2021
Accepted 1 December 2021
Available online 5 December 2021

Keywords:
Rock avalanche
Rockslide
Rock slope deformation
Holocene
Norway

ABSTRACT

Large rock slope failures are temporal processes which act to modify the landscape after glacial retreat. The slope failure process often shows a lag time of thousands of years after deglaciation, with multiple failure events possible. While global datasets constrain this lag time from extensive mapping and dating of paraglacial rock avalanches, the timeline is poorly refined in northern Norway. We present a case study of multiphase failure at Skredkallen on Vanna, one of a group of coastal islands in Troms, northern Norway. The site contains an actively deforming rock slope above a large rock avalanche deposit. The rock slope deformation (RSD) is a system of fractured and dislocated blocks up to 3 Mm^3, and is moving slowly ~5 mm/yr downslope to the north-east. The metasedimentary rock mass contains four pervasive joint sets and a foliation, contributing to a compound structure failure mechanism. The rock mass is further weakened by foliation-parallel sheared mylonite, and the presence of a brittle fault in the immediate area, with evidence of hydrothermal fluid flow though the RSD.

The rock avalanche deposit below the slope deformation is calculated to be 3 Mm^3, and extends >1 km from the source area, displaying typical mobility for north Norwegian rock avalanches onto undrained sediments. The deposits showcase exceptional lobate morphology with elongated ridge-and-furrow features. Raised shorelines predating and postdating the deposit provide temporal constraints on the deposit and an opportunity to reconstruct a relative timeline for the slope evolution. The postglacial marine limit (>14 cal. ka BP) is obscured by the deposit, while shorelines corresponding to the early Younger Dryas (12.2 cal. ka BP) and the subsequent Tapes transgression maximum (7.6–7.2 cal. ka BP) are prominent across the deposits, implying that the avalanche was emplaced between 15 and 12.2 cal. ka BP. Failure occurred during a time of immense climate instability at the boundary to the early Holocene, consistent with global reports of mountain slope failure following glacial retreat. The avalanche was emplaced into what would have been the marine environment. The anomaly between the rock avalanche source area volume (35 Mm^3), and the rock avalanche deposit implies previous failure events, the deposits of which were either removed due to failure of the underlying marine sediments into the fjord, by retreating glacial ice or scour. The initiation of movement at the RSD may be attributed to periods of local climate changes, such as the Holocene Thermal Maximum. Cosmogenic nuclide dating is suggested as the next step to fill gaps in the slope evolution story through the mid to late Holocene.

1. Introduction

Large unstable rock slopes which deform slowly under gravity pose a hazard to mountain communities when they transform from slow creeping movements to rapid rock slope failure. The failures can result in rock avalanches which can entrain large volumes and travel extraordinary lengths (Hermanns and Longva, 2012). The failure process leading to a rock avalanche can be protracted, with sliding and extensional surfaces forming along pre-existing structural discontinuities (Glastonbury and Fell, 2010; Rechberger et al., 2021; Vick et al., 2020a, 2020b). The transformation to avalanche marks the climax of an incremental, temporal failure process (Stead et al., 2007; Hermanns and Longva, 2012; Dick et al., 2013; Stead and Eberhardt, 2013). Seemingly spontaneous failures, or failure as a result of a minor trigger, are the result of paraglacial time-dependent mechanisms progressively lowering the rock slope strength towards failure (Grämiger and Gischig, 2018; Hilger et al., 2020; McColl, 2012; Preisig, 2020; Yerro et al., 2016). A lag time is seen from deglaciation

* Corresponding author.
E-mail address: louise.m.vick@uit.no (L.M. Vick).
[1] Present address: Nordland Fylkeskommune, Markveien 36, 8400 Sortland, Norway.
[2] Present address: LNS AS, Dragnesveien 53, 8484 Risøyhamn, Norway.
[3] Present address: Department of Biology — Microbiology, Aarhus University, Ny Munkegade 116, 8000 Aarhus C, Denmark.

https://doi.org/10.1016/j.geomorph.2021.108069

to the first increase in failure frequency in many regions. This lag time has been termed 'pre-failure endurance' (Ballantyne, 2002) and is linked to the occurrence of large landslides globally which occurred >1000 years following deglaciation (e.g. Le Roux et al., 2009).

Geochronological studies from south western Norway contradict this lag time trend (e.g. Schleier et al., 2017a, 2017b; Hermanns et al., 2017). Böhme et al. (2015) reviewed the temporal distribution of 108 deposits in Storfjord, western Norway. They note a rapid slope response with highest frequencies of failure immediately following local ice retreat between 13 and 11 cal. ka BP and a constant low rate of failure from 9.0 ka BP. In some cases rock slope failures covered valley-ice (Schleier et al., 2015a, 2015b). Evidence suggests that large slope failures may have a destabilising effect on the remaining rock slope, leading to subsequent failures (Hermanns et al., 2006), and many slopes which fail immediately also show failure activity later in the Holocene (e.g. Hermanns et al., 2017). Periods of heightened activity are often linked to the Holocene Thermal Maximum (HTM, 8–4.5 ka) in studies focused on linking recurrences with contemporaneous climate trends (Ballantyne et al., 2014; Böhme et al., 2019; Hermanns et al., 2017; Hilger et al., 2018; Ivy-Ochs et al., 2009; Kim et al., 2004; Pánek, 2015; Prager et al., 2008; Stoffel and Huggel, 2012; Worsley, 1998; Zerathe et al., 2014).

Placing slope failures into a temporal context allows for interpreting the dynamic slope evolution in response to Holocene climate events, and for further refining slope hazard assessment. While the chronology of glacial retreat and related events is well established for northern Norway, little is known about the onset of deformation and the timing of rock slope failures. More than 130 rock slope deformations (RSDs) are identified in the Troms and Finnmark County (NGU: Geological Survey of Norway, 2021a), yet scant work is published which places large rock slope failures in the context of deglaciation and climate.

Some catastrophic failures in the Troms and Finnmark region are dated to shortly after the Younger Dryas (raised shoreline dated to 12.2 cal. ka BP), e.g., the Grøtlandsura avalanche (lat 68.908, long 17.524) which is dated to 11.4 cal. ka BP (Fenton et al., 2011), and the Russenes avalanche (lat 69.2147, long 19.4715) which is dated to 10.9 cal. ka BP (Blikra et al., 2006; Fenton et al., 2011). In contrast the nearby Høltinden (lat 69.1781, long 19.3163) failed in a series of three catastrophic events much later in the Holocene, between 6.1 and 3.3 cal. ka BP (Fenton et al., 2011).

Several of the identified unstable slopes (not yet failed) are shown to have begun deformation during the HTM (Hilger et al., 2020). For instance, terrestrial cosmogenic nuclide dating of sliding surfaces at Nordnesfjellet and Gamanjunni-3 show movement initiation from 6.5 and 5.3 ka, respectively (Blikra and Christiansen, 2014; Böhme et al., 2019). Sliding rates decelerated after the HTM, but currently appear to be accelerating once again as a consequence of global warming (Böhme et al., 2019). This underscores the importance of increasing our understanding of rock slope response to climate variability.

Rock slope failures which form a rock avalanche typically display high mobility. Their deposit, morphological features, and extent are indicative of the geodynamical emplacement process (Belousov et al., 1999; Dufresne and Davies, 2009; McDougall and Hungr, 2005; Schleier et al., 2017a).

In addition rock-avalanche deposits in a postglacial landscape provide relative dating opportunities due to isostatic rebound and their relationship with glaciogenic sediments (Schleier et al., 2015a, 2015b; Schleier et al., 2017a).

We present a case study of a multi-phase postglacial rock slope failure with a distinct morphology, at Skredkallen, (lat 70.170845, long 19.869739; Fig. 1). The site is located on the east coast of Vanna Island (or Vannøya), in Troms and Finnmark County, northern Norway.

The slope contains an RSD in the upper reaches, with clearly displaced bedrock along sharp backscarps, wide tension fractures and steep bounding cliffs. Rock avalanche deposits cover the lower slope and coastal flat. The avalanche deposits have a characteristic blocky, rubbly appearance and sharp margins (Fig. 2).

The goals of this paper are to examine the RSD failure mechanism and to determine the timing of the rock avalanche events. To examine

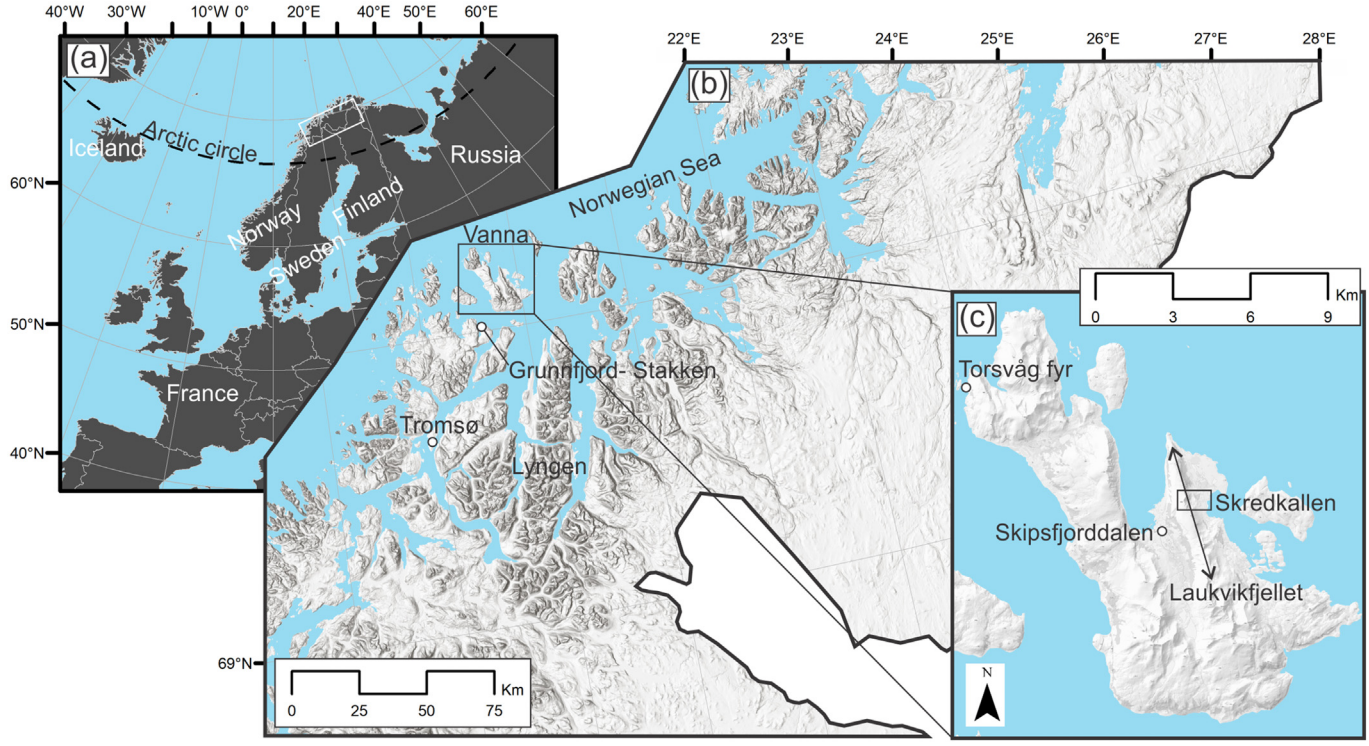

Fig. 1. Location of the study area. (a) Region (white box) in the context of the European continent. (b) Troms and southern Finnmark topographic regions (ESRI world hillshade portal). (c) Detail of Vanna (NMA: Norwegian Mapping Authority [Kartverkert], 2021) showing Skredkallen case study area. White circles in (b) and (c) indicate locations mentioned in this work; arrow shows the ridgeline, Laukvikfjellet.

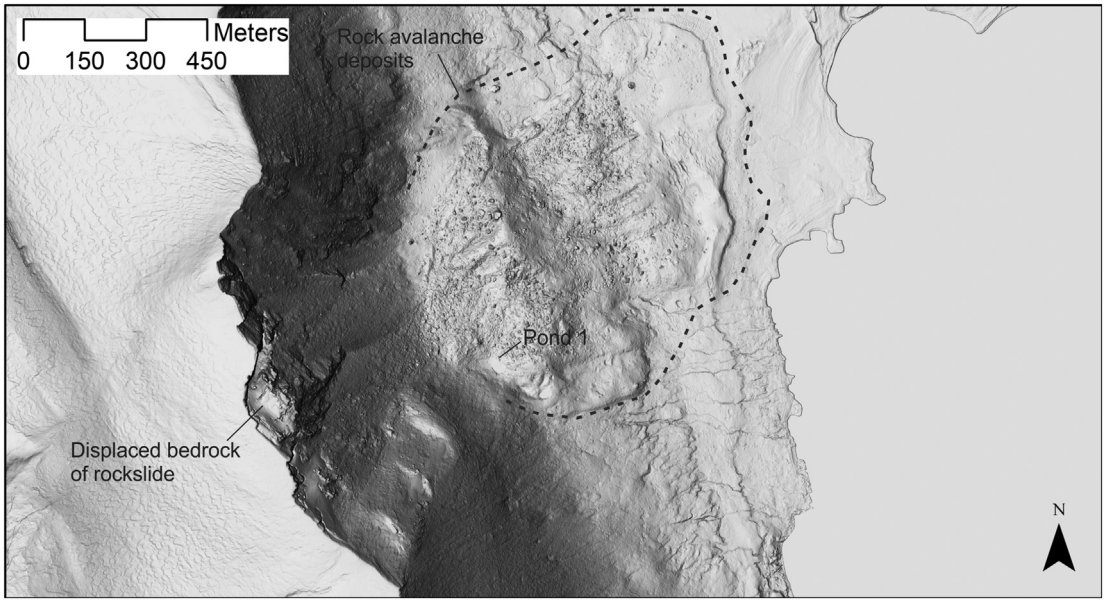

Fig. 2. The site are of interest, multiaspect hillshade based on 0.5 m Lidar (NMA: Norwegian Mapping Authority [Kartverket], 2020).

the failure mechanism, we have mapped and interpreted morphostructure, lithology, structural geology, volume, and velocity. To determine timing of the avalanche we have mapped the deposit and surrounding morphology, interpreted deposit emplacement characteristics, and analysed the postglacial and Holocene evolution of the slope. We examine the relationship between raised shorelines and the deposit, and apply radiocarbon dates obtained from a lake sediment core from a small pond situated on the upper part of the deposit to reconstruct a sequence of events.

2. Setting

2.1. Climate and process regime

The island of Vanna lies in the archipelago to the north east of Tromsø (Fig. 1b) and is characterised by a relatively mild and wet climate (Verpe Dyrrdal et al., 2020). The mean annual air temperature (1991–2020) at the closest meteorological station (Torsvåg fyr, 16 km NW of Skredkallen) is 4.7 °C, with warmest and coldest mean monthly temperatures of 11.3 °C (July) and − 0.4 °C (February), respectively (MET Norway: Norwegian Meteorological Institute, 2021). Mean annual precipitation at nearby Grunnfjord — Stakken (20 km SW of Skredkallen) is 907 mm (1991–2020; MET Norway: Norwegian Meteorological Institute, 2021). The NE (Skredkallen) side of the island is openly exposed to the Norwegian Sea, frequently facing strong wind. The mean tidal range is 173 cm (NMA: Norwegian Mapping Authority [Statens Kartverket], 2021).

The island is mostly treeless, with low-lying bogs and heath vegetation. The island is outside of the lower limit for mountain permafrost (Gisnås et al., 2017), although relict permafrost features are observed at a similar latitude on neighbouring islands indicating it has been present in past colder periods (Lilleøren et al., 2012). The existence of bedrock fracture ice is not discounted (cf. e.g. Blikra and Christiansen, 2014). A holiday cabin sits at the toe of the slope (Fig. 3), which is a

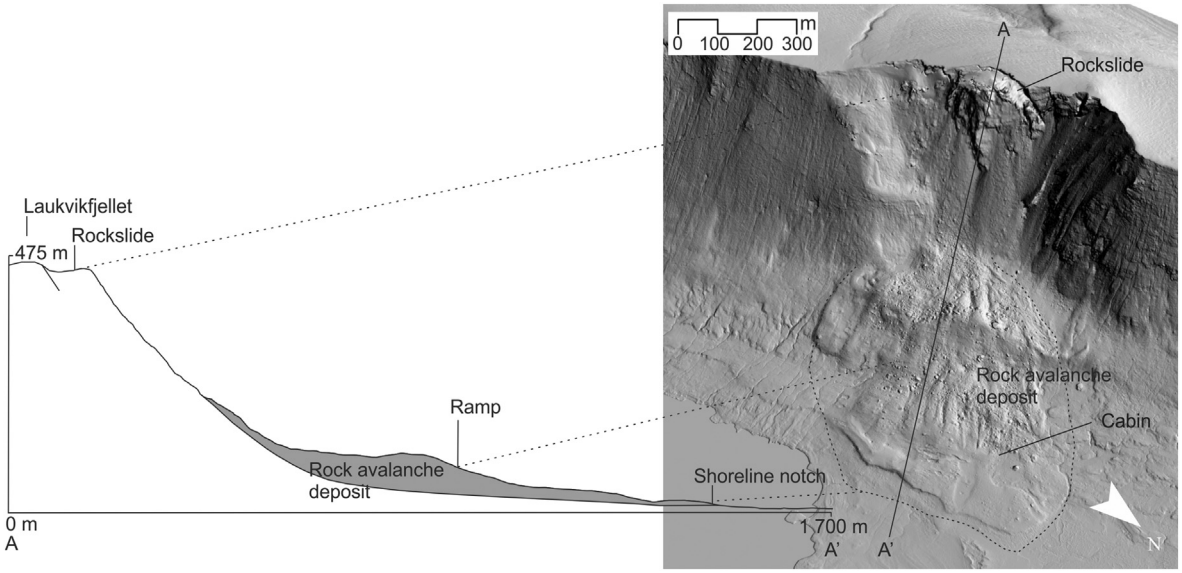

Fig. 3. Site overview. Longitudinal section of the site area and 3D hillshade draped on 0.5 m Lidar (NMA: Norwegian Mapping Authority [Kartverket], 2020).

popular hiking area for local residents. The cabin unoccupied parts of the year.

2.2. Geomorphological overview

Vanna has an alpine landscape, with steep mountain slopes, U-shaped valleys and deep fjords. The mapping area is crosscut by a NW-striking ridgeline, Laukvikfjellet (482 m asl) (Fig. 1c). The geliflucted ridgetop slopes 35° down to a wide strandflat of marine deposits, sandy beaches and small islands. At c. 150 m asl the slope flattens out gently towards the sea in a platform of raised marine sediments, some outcrop ridges and widespread peat bogs. The avalanche deposits cover a large area from the toe of the slope and across the platform of raised sediments. Pond 1 (Fig. 2; lat 70.1693, long 19.8693) measures 0.8 km^2 and is located at 101 m asl, on the rock avalanche deposits (Fig. 3). The lake is dammed by a local high point 'Skredkirka' [Norwegian: The Avalanche Church] behind a ramp, and is likely fed by groundwater seepage, snowmelt and precipitation flowing through subsequent ponds and onwards to the bay. A series of small streams are found at the slope break to the coast flat, and flow across the platform.

2.3. Bedrock geology

The bedrock of Vanna is part of the Precambrian basement complex of tonalitic, granitoid and quartz-dioritic gneisses in western Troms, overlain to the east by allochthonous Caledonian rocks (Bergh et al., 2007, 2010). The Skredkallen site is comprised of Skipsfjord Nappe rocks, a succession of Precambrian thrust sheets with tonalitic gneisses and lenses of mafic intrusive sills (Opheim and Andresen, 1989; Paulsen et al., 2020). These rocks are well foliated and include many foliation-parallel mylonitic shear zones (thrusts) that dip gently NW, and associated complex internal folds (Bergh et al., 2007). In addition, Skredkallen is bound to the north by a major brittle normal fault, the Skipsfjord-Slettnes fault (first mapped by Paulsen et al., 2020) which dips steeply SE. This fault is part of a regional system of Mesozoic NE-SW striking coast-parallel and NW-SE striking oblique normal faults and related steep fracture sets, linked to rifting and opening of the North-Atlantic Ocean (Indrevær et al., 2013; Koehl et al., 2019).

2.4. Quaternary geology

Vanna was deglaciated between 15 and 14 cal. ka BP (Romundset et al., 2011). The island is located between the maximum extent of the Late Weichselian ice sheet and the Younger Dryas (YD) moraine (Andersen, 1968; Corner and Haugane, 1993). Glacioisostatic adjustment still acts in the Troms region and the area currently experiences an uplift rate of 1–1.5 mm/yr (Romundset et al., 2011). The postglacial marine limit (ML) on Vanna, is identified as a distinct raised shoreline at Skipsfjorddalen immediately west of Skredkallen at around 47 m asl in the area of interest (Corner and Haugane, 1993). Two additional shorelines form distinct morphostratigraphic markers: the 'Main' and 'Tapes' shorelines. The Main shoreline formed during the YD and lies at an elevation of c. 22 m asl (Corner and Haugane, 1993). In many localities it is observed as a terrace in bedrock. It has an early and late stage age of 13.2 and 11.2 cal. ka BP (cf. Andersen, 1968). In this contribution we choose to represent it as the median age of 12.2 cal. ka BP (the 2σ age ranges for these bounding dates span 13.8–10.2 cal. ka BP). The Tapes shoreline (12 m asl) was formed during the Tapes transgression maximum in the Middle Holocene, dated to the equivalent of 7.6–7.2 cal. ka BP in Lyngen (45 km SE of Skredkallen) by Corner and Haugane (1993). Sea-level history at Vanna can be inferred from a previous relative sea-level curve for Vanna (Corner and Haugane, 1993), updated by comparing it with results from a comparable locality at Sørøya, Finnmark, to the north-east (Romundset et al., 2011) and proportionally adjusting the shape and elevation of the curve using the elevation of the regionally distinct Main and Tapes shorelines as reference levels (Fig. 4). The results show the following likely trend in relative sea-level change at Vanna since deglaciation: 1) a rapid relative sea-level fall from about 45 to 20 m asl during initial glacier retreat and rapid isostatic rebound between c. 14–15 and 12.2 cal. ka BP; 2) a slow rate of fall during formation of the Main shoreline and local glacier readvance around 12.2 cal. ka BP, 3) a rapid rate of fall from about 20 to 8 m asl during continued deglaciation between 11.8 and 9 cal. ka BP; 4) a gradual sea-level rise of c. 2 m during the Tapes transgression between 9 and 7.2 cal. ka BP; and 5) a slow sea-level fall from the Tapes shoreline after 7.2 cal. ka BP.

Surficial deposits mapped at 1:250,000 shows that the rock avalanche deposits likely overlie marine deposits of the strandflat (Fig. 5).

3. Methods

3.1. Desktop and field mapping

Geomorphic mapping was performed using the ArcticDEM 2 m resolution hillshade (Porter et al., 2018) and field mapping. Mapping was subsequently updated with the publication of 2 pt/m^2 Lidar, which enabled more detailed geomorphic analysis (NMA: Norwegian Mapping Authority [Kartverkert], 2020). Orthographic photos were obtained from Norge i bilder (NMA: Norwegian Mapping Authority [Kartverket], 2021). Additional aerial images were taken with UAV from DJI Inspire drone with a 12-megapixel Zenmuse Z3 camera mounted. Field mapping was conducted over 4 summer seasons between 2017 and 2019 as part of two masters projects (Mikkelsen, 2019; Trønnes,

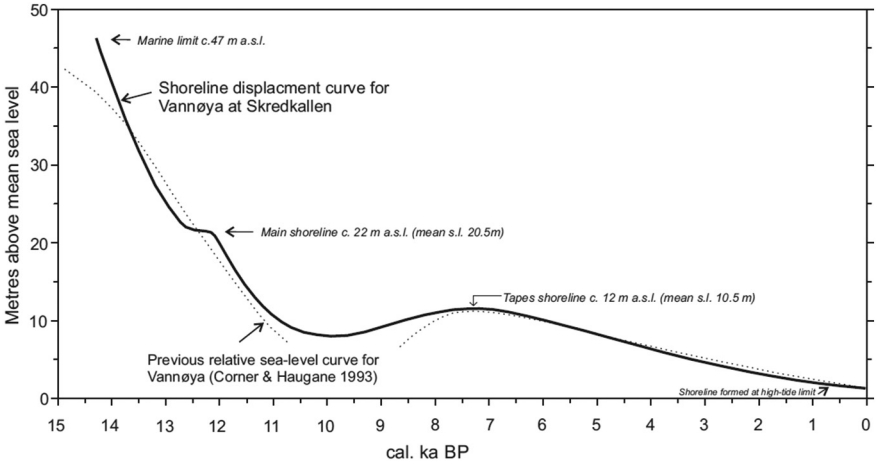

Fig. 4. Shoreline displacement curve for Vanna (Vannøya) at Skredkallen, modified partly from a comparable locality at Sørøya, Finnmark (Romundset et al., 2011) and adjusted elevationally using the Main and Tapes shorelines as reference levels. The dotted line shows a previous sea-level curve for Vanna (Corner and Haugane, 1993).

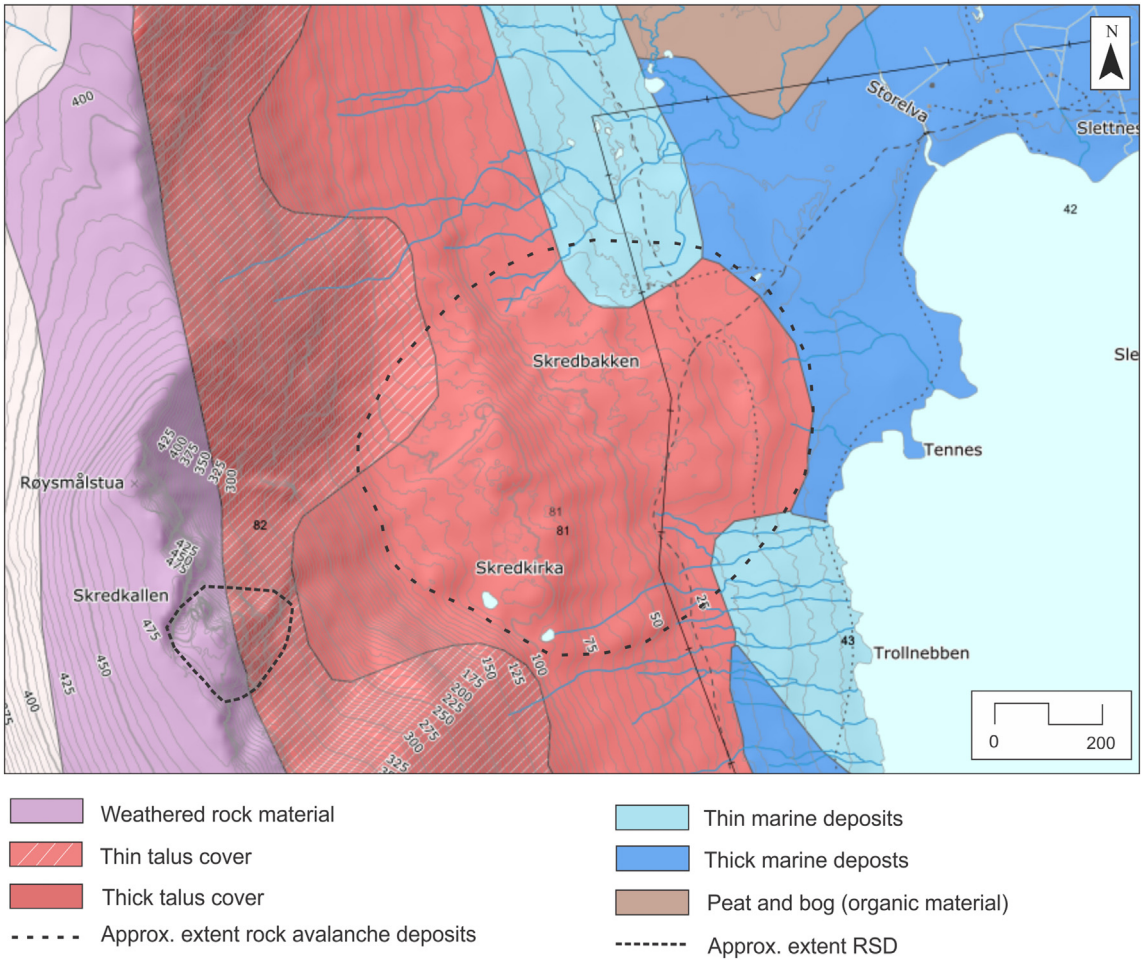

Fig. 5. Surficial deposits map of the site area taken from map viewer, (NGU: Geological Survey of Norway, 2021b) and translated from Norwegian. Approximate extents of the RSD and rock avalanche deposits have been added. Note that 'marine deposits' denotes undistinguished sea, fjord and beach deposits.

2019). Surficial material presented in the national database (NGU: Geological Survey of Norway, 2021b) were ground-truthed where possible by means of sediment pits and surface clast size measurements. Sediment pits were excavated with a hand held shovel and logged stratigrpahically. Raised shorelines were mapped from hillshade and further refined in the field by tracking with a hand-held Garmin 62 s GPS device.

Inferometric Synthetic Aperture Radar (InSAR) measurements were extracted from the InSAR Norway, a free and open InSAR mapping service (www.insar.ngu.no; NGU: Geological Survey of Norway, 2018). The measurements used are point based ground movement measurements from 2015 to 2020 Sentinel-1 satellite images processed with a Persistent Scatterer Interferometry algorithm (Ferretti et al., 2000, 2001). It should be noted that InSAR maps show point-based ground surface mean velocities corresponding to changes in sensor-ground distance, i.e. displacement along the radar line-of-sight (LOS), depending on the satellite acquisition geometry. For more information about the potential and limitations of InSAR for the characterisation of RSDs, see e.g. Barboux et al., 2015. Measurements of Skredkallen downward movements were derived from Sentinel-1 Ascending track 3 data in the ENE direction. The satellite line of site azimuth is 74.1° at an incidence angle of 31.82°. InSAR data was summarised for the main downthrown terrace of the Skredkallen rockslide using the polygon tool (a mapping service tool which summarises average line of site velocities within a specified polygon area).

Bedrock and structural data were collected in the field using a combination of traditional methods (e.g., compass) and mobile phones app GeoID v1.8 (the latter verified against a compass). Stereonet analysis of 304 measured structural data points was performed in RocScience Dips 7.0 using 1σ viability cone about Fisher contour pole clusters in lower hemisphere equal area projection. Orientation data are given in 'dip direction/dip' format.

3.2. Volume and runout analysis

Volume estimation of the RSD, source area and rock avalanche was derived from 3D modelling in the dynamic 3D modelling software Leapfrog Works 2021.1.3 (Seequent, 2021). We created new artificial mesh surfaces based on proposed feature extents in 3D space to cut or fill the DEM and generate shape volumes.

The rock avalanche mobility at Skredkallen was compared to global and Norwegian empirical datasets. Scheidegger (1973) presented a population of global rock avalanches with measured volumes (v) and angle of reach (θ; angle of a line projected from the backscarp to the deposit front). The best-fit curve for this dataset was given as $\tan\theta = 4.209 \cdot v^{-0.15666}$. It was later determined that Norwegian case studies fall within the envelope of data presented by Scheidegger, but are typically concentrated in the lower mobility end of the envelope (Hermanns et al., 2012). Recently, a much larger dataset of Norwegian rock avalanches has been added (Velardi et al., 2020), with new formulas representing populations of rock avalanches onto various substrates, and in both northern and southern areas of Norway. These show that mobility of rock avalanches onto e.g. ice and marine sediments have higher motilities than inferred by the Scheidegger curve. In addition, rock avalanches in northern Norway tend to have higher nobilities due to the comparatively more open valley landscape. Velardi et al. (2020)

proposed a best-fit curve for rock avalanches onto marine sediments of $\theta = 18.311v^{-0.039}$.

3.3. Lake sediment coring and chronology

In March 2019 one lake sediment core was retrieved from the frozen surface of Pond 1 using a 100 cm long Russian corer (diameter 7.5 cm). Sixty cm of sediment was retrieved, below which the presence of rocky material hindered further penetration. The core was visually described for its lithostratigraphy. The sediment core had a high organic content (e.g., preserved mosses and terrestrial plant (leaf) material), without any clear stratification. The lowermost 5 cm of the sediment core was more minerogenic and contained pebbles of up to 1 cm.

The aim of the coring was to provide a minimum age for the rock avalanche, by obtaining the basal age of the lake sediments. Because of the shallow depth of the pond some reworking of the sediment due to freeze-thaw cycles might be expected. To check for possible disturbance, four plant macrofossil samples were taken at 23–24 cm, 39–40 cm, 55–56 and 57–58 cm depth. The uppermost sample consisted of terrestrial leaves and the lowermost three samples were mixed samples of leaves and mosses. As the bedrock in the area consists of tonalitic gneisses with no limestone or marble, no lake reservoir effects are expected, and submerged mosses are regarded as reliable radiocarbon dating material. All samples were measured by means of accelerated mass spectrometry (AMS) radiocarbon dating at the Ångström Laboratory at Uppsala University, Sweden.

3.4. Date calibrations

The online Calib 8.2 calibration program (Stuiver et al., 2021) and the IntCal20 and Marine20 calibration curves (Reimer et al., 2020) were used for calibration of the radiocarbon ages reported from previous studies as well as those presented here. All ages in the text are given in calibrated kiloyears before present (cal. ka BP; BP = 1950 CE), and presented as calibrated median values using the 95.4% probability ranges.

An age-depth model for the sediment core from Pond 1 was established using the Bacon package (v. 2.5.0) and IntCal20, running in the open-source statistical environment R (v.4.0.3; R Core Team, 2020). The age-depth model was constructed using the following parameters: acc.mean = c(25,30), acc.shape = 2.7, mem.mean = 0.38, mem. strength = 45, boundary = 30, d.max = 60. The age of the surface sediments was set to year of sampling (2019 CE), and since the uppermost 10 cm were water saturated, an uncertainty of 20 years was assumed for the uppermost sediment layer in the age-depth model.

4. Results

For the purposes of description the areas at Skredkallen are subdivided into the RSD, which comprises an area designated as a rockslide; and the rock avalanche deposit on the lower slope (Fig. 6). While describing both sections we refer to the portion of the slope which supplied both the rock avalanche and the RSD as the 'source area'. We first describe the geology and structure of the RSD, and then relate the structure to the geomorphology of the RSD area in order to make an assessment of the failure mechanism and potential failure volume. We then describe the geomorphology and volume of the rock avalanche deposit, as well as results of the age-dating.

4.1. Rock Slope Deformation (RSD)

4.1.1. Geology, structure and morphostructure

The bedrock at Skredkallen is part of the Skipsfjord Nappe (Opheim and Andresen, 1989), predominantly composed of tonalitic gneiss with mylonitic foliation, intercalated with numerous mafic sills (Fig. 7). The tonalitic gneisses are homogenous and show little variations both in colour and texture, although plagioclase and quartz content vary locally. In some places sheared zones of mylonite run parallel with the dominant foliation (Fig. 7b). The shear zones are associated with thrusts which emplaced the Skipsfjord Nappe (Paulsen et al., 2020). They formed at lower amphibolite-facies metamorphic conditions, but were reactivated and retrograded during low-grade metamorphism producing local semi-ductile cataclasites along shear zone surfaces (Fig. 7b). These horizons vary from 10 to 50 cm in thickness. They are brown-coloured and in some places soft and heavily weathered.

The Laukvikfjellet ridgeline is crosscut by a NE-SW-striking normal fault (Paulsen et al., 2020) (herein termed the Skipsfjord-Slettnes Fault) which shows variable (20–50 m) offset and defines the northern boundary of the source area (Fig. 6A). While no fault gouge or other evidence of brittle cataclasis is observed at the surface, 20–50 m of vertical offset is seen along the plateau and is observable in hillshade and orthographic perspective (Fig. 2; Fig. 3). Four main joint sets are mapped,

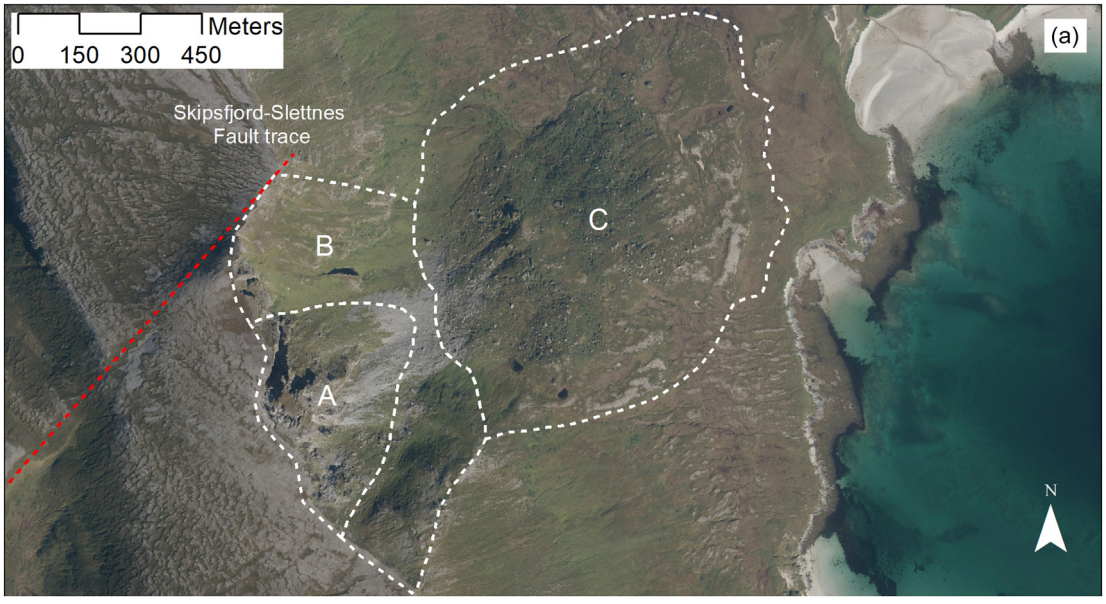

Fig. 6. Areas of interest in the study area for context, overlaid on aerial (NMA: Norwegian Mapping Authority [Kartverket], 2021). A = Rockslide area. A + B = Source area for the rock avalanche deposits. C = Rock avalanche deposit. Skipsfjord-Slettnes Fault trace after Paulsen et al., 2020.

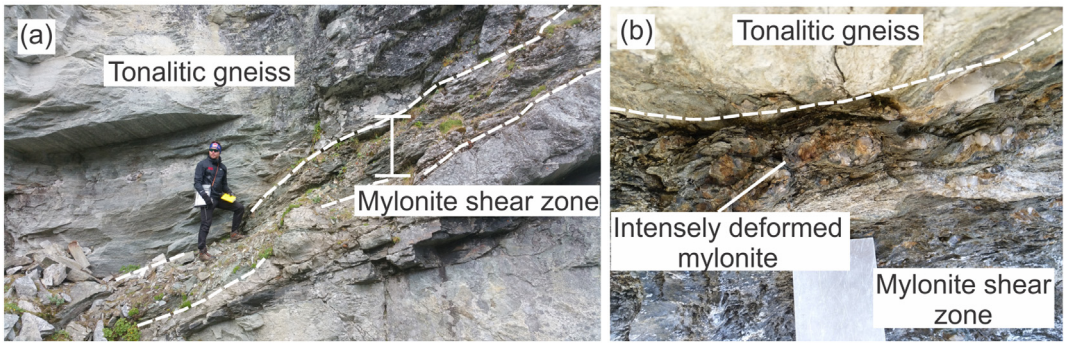

Fig. 7. Typical bedrock geology observed at outcrop scale in the rockslide area. (a) Weakly foliated tonalitic gneiss, with a foliation-parallel mylonitic shear zone. (b) Close-up image of the transition between the mylonite zone in Fig. 6A and relatively unaffected bedrock, with internal lenses of degraded and semi-ductile (cataclastic) deformed tonalite at the boundary.

termed J1 to J4 (Fig. 8, Table 1). J1 and J4 were the most dominant joint sets, both near-vertical and dipping towards ESE and SW, respectively. The subordinate joints (J2 and J3) when combined with J1 and J4, respectively, define conjugate joint sets. The dominant foliation in the intact rock is sub horizontal to gently NNE-dipping, daylighting obliquely in the slope. Assuming the foliation is continuous at this orientation, a rotation is seen both in the lower part of the RSD, where foliation dips gently inwards to the WSW, and at Kaillen (a tall column) where the foliation dip is steeper outwards to the NNE (Fig. 8, Table 1).

The RSD source area (Fig. 5a) appears at present as a distinct concavity in the NNW-SSE trending mountain ridge. A 1.2 km-long concave section of the ridgeline delineates the upper scarp of the source. The central 400 m of the source area houses the RSD. It is an area of discontinuous bedrock between 470 and 270 m asl. The sliding mass is offset across major backscarps and contains blocks and columns with flat terraces draped by a thin grassy veneer and delimited at the front by steep cliff faces (Fig. 9a, b).

The main backscarps have been delineated for the actively deforming area specifically (Fig. 10). They strike NW-SE (with a dogleg to the NE) and NNE-SSW. The rock mass has dislocated from the NW-SE striking section of the backscarp, sliding downwards c. 2 m over stepped

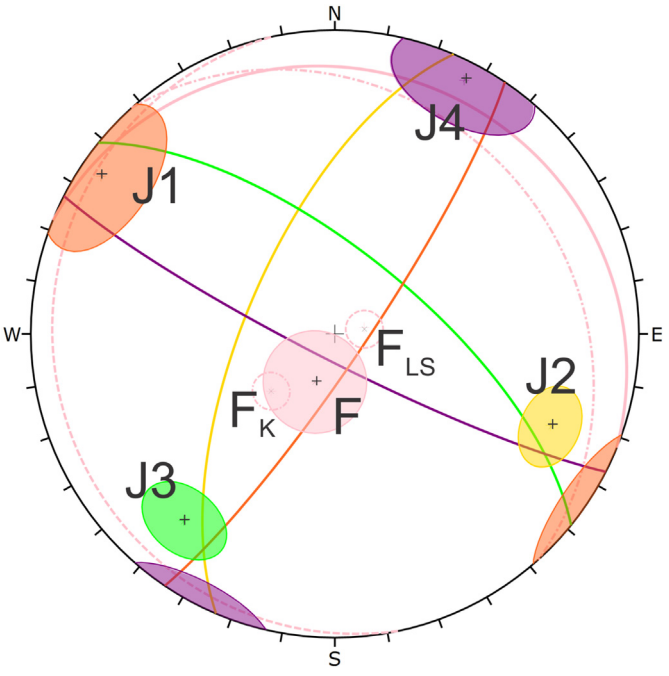

Fig. 8. Stereonet projection of mapped discontinuities. Stereonet in equal area lower hemisphere projection and displays 1 standard deviation cone around the mean set pole. J = joint set, F = foliation, F_{LS} = foliation lower slope, F_K = Kaillen.

subvertical J3 and J4 joint sets. The sliding mass of the RSD is comprised of a system of dislocated blocks. The blocks are delineated by and contain open fracture systems which often zig-zag (Fig. 9a). The systems strike predominantly NE-SW, NW-SE or NNW-SSE, following a similar zig-zag pattern as the backscarp. Those striking NW-SE generally follow joint plane surfaces of J4. Those striking NE-SW follow J3. Some of these are up to 35 m long, indicating high persistence.

The intersection of these fracture systems has created sinkholes where draped soil on the dislocated block surfaces has fallen into the open space between fracture sets. These are typically c. 0.5 m wide and c. 0.25 m deep. Several large, chaotically oriented blocks can be found in gaps between and surrounding the dislocated blocks.

A large trench has opened between the NNE-SSW striking segment of the backscarp and the sliding mass. An up to 60 vertical m section of the scarp is exposed in the trench, made up of J1 and J2. Within the trench a distinctive column, Kaillen (Fig. 9b) tilts downwards towards SE. Snow can be found in the trench opening all year round, especially at the north end, where ice was mapped in the shadows of the backscarp during the summer months.

The front/east side of the RSD is a series of steep scarps and steps. There is no distinct morphological toe in the lower slope. The slope break from the steep scarps and to the top of the rock avalanche is draped in talus sourced from rockfall and deposits from a partial failure reported by residents in the early 1950's (see talus lobes, Fig. 10). At the southern edge of the RSD a 'block field' has been mapped (Fig. 10). This is comprised of large, partly disaggregated blocks which are the result of deformation but appear not to have moved far from the source location. On the south side of the RSD a series of three steps leads from the ridgeline down to the base of the source area (Fig. 9c). These steps follow the bedrock fabric and hint at the geometry of the prehistoric slope failure.

4.1.2. Failure mechanism and movement

The backscarps of the RSD dip steeply downslope and do not daylight in the lower slope. The backscarps themselves are insufficient to effect movement and therefore the sliding surface must be defined by more than one structure. The sliding movement at Skredkallen may be controlled by Foliation and J3 and aided by the deteriorated mylonite shear zones (Fig. 11). Thus, we consider the failure mechanism to likely be complex and in the style of a compound slide (Glastonbury and Fell, 2010, Hermanns and Longva, 2012, Hungr et al., 2014; Vick et al., 2020a, 2020b). It should be noted that this mechanism has not been derived from subsurface data or rock failure modelling.

The volume of the RSD, calculated in Leapfrog Works based on extents proposed in Fig. 11 was calculated to be 3 Mm^3. The RSD is moving downwards to the ENE (direction LOS of the Sentinel-1 ascending 3 track) at a rate of c. 10 mm/yr at Kaillen, and c. 5 mm/yr along the south eastern border of the block. The central and inner parts of the block are in the satellite shadow.

Table 1
Joint set characteristics. Average joint set pole and deviation window determined from Dips analysis of structural measurements (Fig. 8).

Joint set	Spacing	Persistence	Shape	Roughness	Condition/comment
J1 124/82 ± 16.9	0.5–2.0 m	10–25 m	Planar. occasionally listric	Smooth to very smooth	Orange and pink coating (ca. 2 mm thick)
J2 293/68 ± 9.0	0.2–1.0 m	0.5–1.0 m	Planar	Smooth	Orange coating (<2 mm thick)
J3 039/68 ± 10.5	0.2–0.5 m	Predominantly 0.1–0.5, max 25 m	Planar, undulating	Rough	Slope-parallel
J4 207/83 ± 15.5	0.5–1.0 m	0.5–20 m	Planar	Rough	–
Foliation 022/14 ± 13.8	0.05–0.5 m	0.1–2.0 m	Planar	Rough	–
Foliation lower slope 258/08	–		–	–	–
Foliation Kaillen 048/23	–		–	–	–

4.2. Rock avalanche

4.2.1. Geomorphology

The geomorphology of the Skredkallen area is presented in Fig. 12. A large lobe of rubbly rock avalanche material stretches out to the NE for 1400 m from the foot of the Laukvikfjellet slope across the strandflat. The deposits generally decline in thickness with distance from the source area on average at 8° from horizontal (longitudinal section, Fig. 3).

The 1:250,000 surface cover map (Fig. 5; NGU: Geological Survey of Norway, 2021b) depicts the lobe as overlying marine deposits. We have updated this with a 1:5000 geomorphological and raised shoreline map showing surficial cover as it is relevant to the interpretation of the site (Fig. 12). The key materials and shorelines are described below.

Talus.

The non-vegetated talus material (e.g. the lobes, Fig. 10) contains angular boulders ranging up to 2 m diameter. The largest material is found in the middle and lower parts of the talus zone (Fig. 13a). Outside of these lobes the talus zone is vegetated and clast size is not apparent.

4.2.2. Blocky rock avalanche deposits

Blocky rock avalanche deposits are found in the inner portion of the lobe. Boulder sizes range up to 20 m, but are typically 1–5 m in diameter (Fig. 13b, c). The orientation of the clasts, measurable by foliation planes in boulders, appears to be random upon visual inspection. The blocky rock avalanche deposits are vegetated with sparse birch forest cover.

4.2.3. Smooth rock avalanche deposits

Smoother and less vegetated surface material occurs in a concentric pattern around the outer lobe. In these areas (smooth rock avalanche deposits, Fig. 12) the surface material consists of a range of particle sizes from fine matrix material (i.e., silt) to clasts of gravel and small boulders (<1 m in diameter). Sporadically larger blocks can be found within the domain (c. 5 m diameter). Visual observations suggest that the clasts are randomly oriented.

Excavation reveals a silty sand layer overlying a sandy layer containing weathered cobble to boulder-sized clasts of rock material. The relatively finer clast size and occurrence of a fine-grained matrix explains the smoother texture of these areas of the rock avalanche deposit, and could affect the drainage conditions leading to a change in vegetation.

4.2.4. Eroded rock avalanche deposits

The rock avalanche deposits are eroded in windows within the lobe, and ubiquitously in front of the Tapes shoreline (Fig. 15a, b and c). These areas are mapped where sparse rock avalanche debris occurs discretely on marine clay/peat rather than in a typical matrix of material. Typically, only large blocks (>2 m diameter) remain (Fig. 15c), implying finer material has been washed out. This erosion is attributed to fluvial action above the Main shoreline- at the southern flank of the deposits a drainage path from ponds 1 and 2 flows though the eroded furrow. This flow has the potential to move material in times of intense rain, either by flooding or debris/slush flows (Fig. 12). Below the Main shoreline it is attributed to marine erosion as the tidal zone presumably moved relatively lower across the deposit lobe, breaching areas above the shoreline in stormy periods. The sharp notch of the Tapes shoreline delineates an area below which extreme erosion has taken place.

4.2.5. Peat, sand and clay

The area mapped as thick and thin marine deposits (Fig. 5; NGU: Geological Survey of Norway, 2021b) were for the most part identified as peat bogs in the field. The peat contained fine-grained silty sediment with a high organic content.

Some small pockets of sand can be found to the south and east of the deposits. The sand is typically structureless, medium grained interbedded with thin layers of fine sand.

At the northern flank of the lobe an angular bay is notched in to the avalanche material (Fig. 12), attributed to a small slide on the underlying

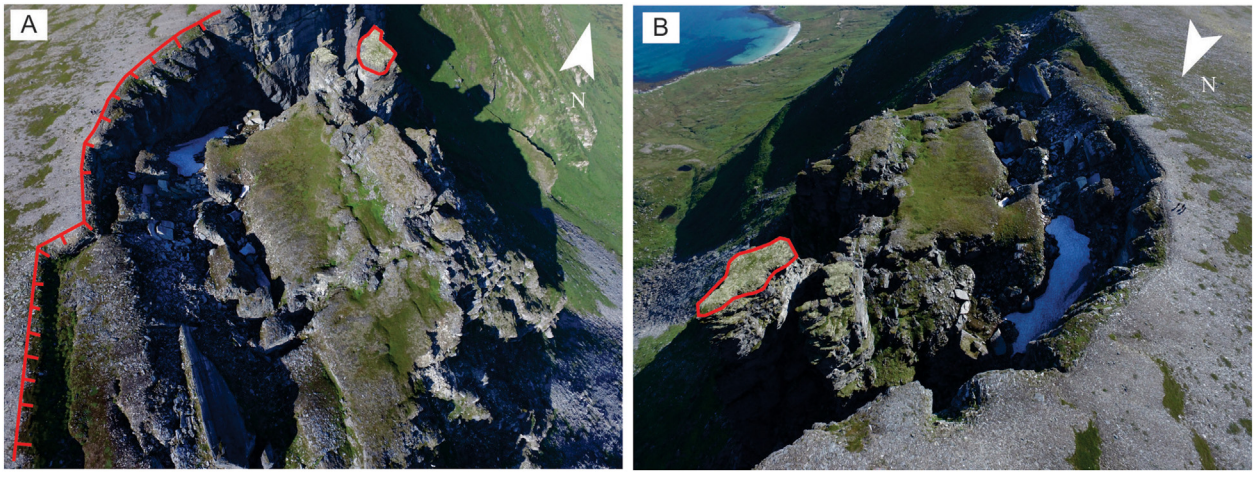

Fig. 9. Perspective images of the RSD. (a) Skredkallen backscarp (red line) delineates the sliding mass below. The block surface of the toppling column, Kaillen, is indicated by the red polygon. (b) Skredkallen as seen from the opposite direction, with Kaillen shown leaning eastwards (block surface depicted by red polygon).

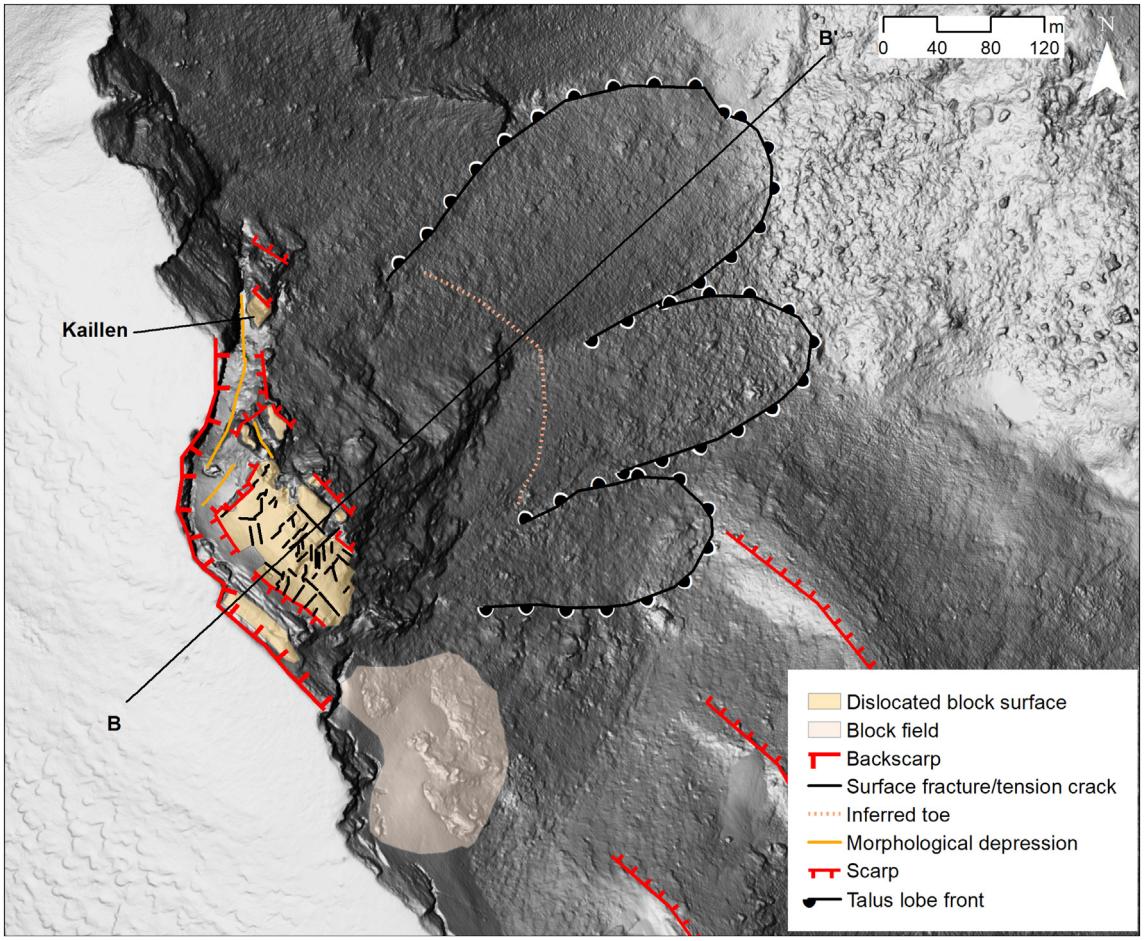

Fig. 10. Morphostructural map of the active RSD area overlaid on the DEM (NMA: Norwegian Mapping Authority [Kartverkert], 2020). Note that smoothed areas around the ridge crest correspond to lingering snow at the time of data acquisition. Inferred toe is conceptual only, not measured, and corresponds to cross section B–B′ (Fig. 11).

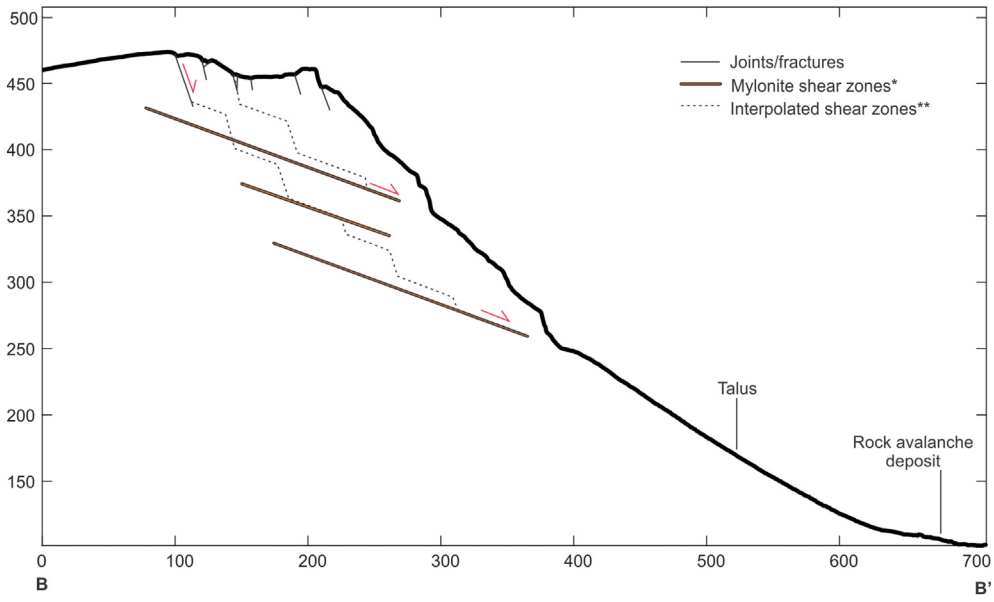

Fig. 11. Conceptual cross section B-B′ of the Skredkallen rockslide area based on Lidar DEM (NMA: Norwegian Mapping Authority [Kartverkert], 2020). See Fig. 10 for location of the profile line. Note that the locations of foliation-parallel mylonite shear zones are approximated, not mapped at these specific locations. **Structures of the 'shear zone' represent joints and foliation surfaces and are also conceptualised.

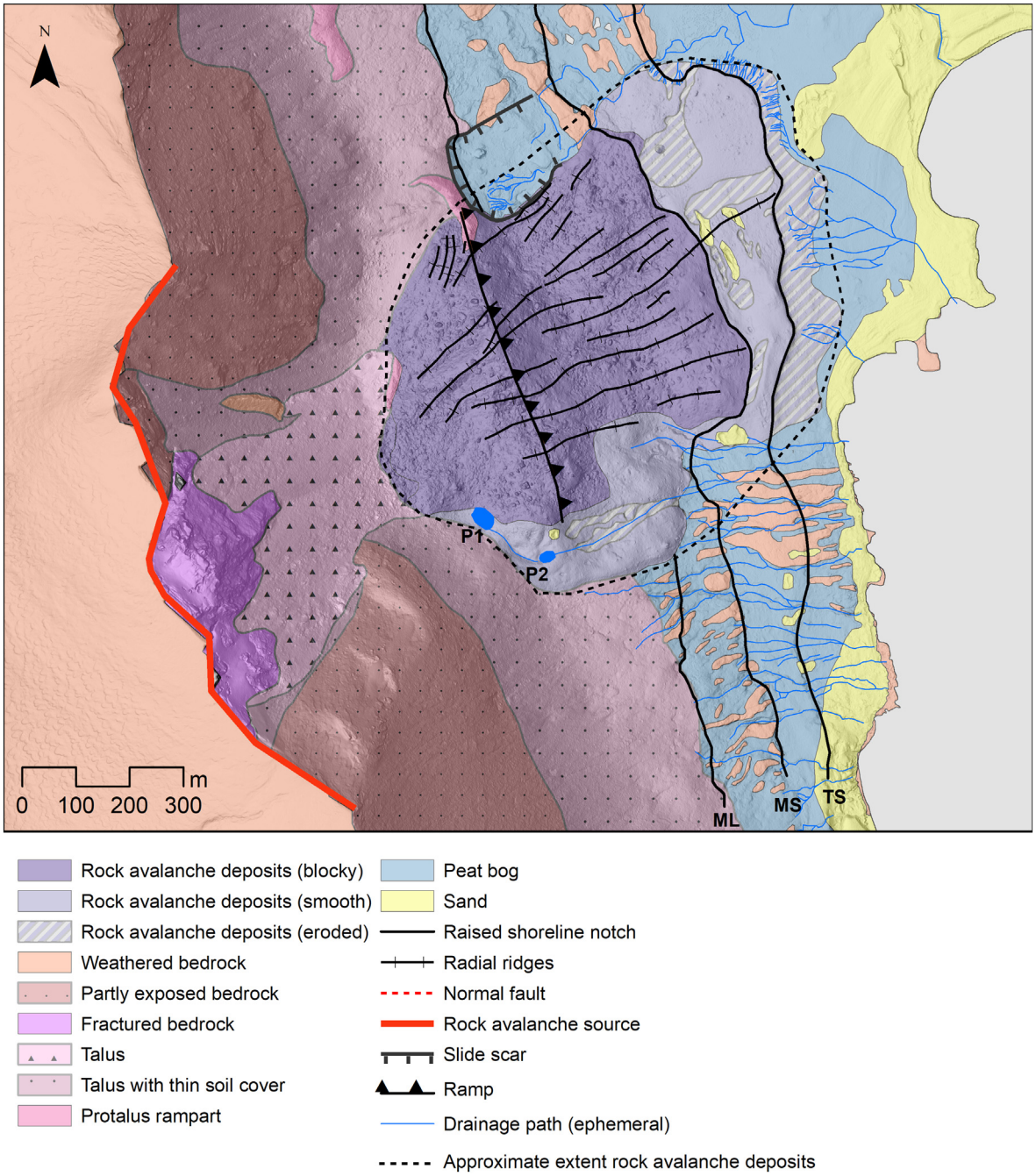

Fig. 12. Geomorphological map of Skredkallen (overlaid on mulitaspect hillshade (NMA: Norwegian Mapping Authority [Kartverkert], 2020). ML = Marine limit, MS = Main shoreline, TS = Tapes Shoreline, P1 = Pond 1, P2 = Pond 2.

marine clay, notable in the area for its low shear strength when disturbed (e.g., Gebremedhin Nigussie (2013)).

4.2.6. Raised shorelines and lineations

No evidence of the Marine Limit (ML) is seen within the deposit lobe boundary; however it can be traced as a subtle notch in the landscape running in both the north and south directions from the deposit at around the same elevation of the base of the ramp. The Main shoreline clearly separates smooth from blocky rock avalanche deposits at the outer lobe (Fig. 15b), and the Tapes shoreline is a sharp notch separating smooth from eroded rock avalanche deposits at the front of the lobe (Fig. 15d).

The surface of the rock avalanche deposits is lineated, with elongated ridges and intervening furrows diverging downslope somewhat from the foot of the main slope towards the edge of the lobe (Fig. 12). The elongated ridges are mostly continuous and up to 800 m long with some breaks and typically between 4 and 8 m high. The largest blocks in the deposit tend to be concentrated along the ridges.

4.2.7. Volume and runout

The volume of the source area and rock avalanche deposits were calculated in Leapfrog Works using extents delineated in Fig. 6 are 35 Mm^3 and 3 Mm^3 respectively. These show a considerable difference, especially when accounting for volumetric bulking of the rock avalanche from entrainment of the loose marine sediments (Aaron and McDougall, 2019; McDougall and Hungr, 2005).

The run-out distance (L = 1400 m), measured as the distance from the backscarp to the eroded rock avalanche material at the front of the

Fig. 13. (a) Looking up at the Talus lobes under the RSD (note dog for scale, black circle). (b) Blocky rock avalanche deposits on the ground. (c) Blocky rock avalanche deposits and Pond 1, looking SE.

deposit lobe. The height difference (H = 460 m) is measured as the difference in elevation between the backscarp and the front of the deposit. These parameters give an H/L of 0.3 or angle of reach of approximately 19°. In comparison with global data, the avalanche runout exceeds the mobility for a 3 Mm^3 avalanche which according to (Scheidegger, 1973) should be 22° (note that Scheidegger's relationship has a correlation coefficient of 0.82). However the angle of reach falls more closely to the best-fit line for avalanches onto marine sediments: according to (Velardi et al., 2020) should be 18°. Note that the latter is based on only 4 data points, and the correlation coefficient is not specified.

4.2.8. Lake sediment dating

While the rock avalanche geomorphology and relationship with raised shorelines allows an approximate temporal constraint, more concrete ages were required to refine the timeline of the site evolution. Sediments from Pond 1, on the upper rock avalanche deposit lobe (Fig. 12), were cored for the purposes of extracting stratified organic material for ^{14}C dating. The analysed samples resulted in a fairly linear age-depth model (Fig. 16), indicating continuous organic deposition in the pond basin from 1.7 cal. ka BP (Table 2), providing a minimum age for rock avalanche activity.

5. Discussion

This paper spans a wide range of topics, including the rock slope failure deformation mechanism from a bedrock perspective; geomorphology of a rock avalanche deposits; and failure timing determined by relationships between the avalanche deposits, postglacial shoreline modification and stratified lake sediments. The intention has been to provide insights into the evolution of the slope environment at eastern Vanna since deglaciation. To that end, we now present a discussion on the deformation mechanism, the timing of events, emplacement conditions of the rock avalanche, and place these in the large context of progressive rock slope failure and slope evolution.

5.1. RSD deformation mechanism

The rock slope system at Skredkallen indicates an iterative and ongoing failure processes operating, with an active RSD and failure deposits

Table 2
Radiocarbon ages from Pond 1, Vanna. The basal age is inferred based on extrapolation below the lowermost radiocarbon age.

Lab ID	Sample	Dated material	$\delta^{13}C$ (‰ VPDB)	Depth (cm)	^{14}C age (BP)	Calibrated 2σ age range (cal. a BP)	Median age (cal. a BP)
Ua-62818	VAN 23–24	Leaves	−26.0	23–24	257 ± 27	280–489	384.5
Ua-62819	VAN 39–40	Mosses, leaves	−25.0	39–40	1117 ± 27	912–1118	1015
Ua-62820	VAN 55–56	Mosses, leaves	−25.0	55–56	1688 ± 28	1483–1662	1572.5
Ua-62821	VAN 57–58	Mosses, leaves	−25.8	57–58	1731 ± 27	1549–1723	1636
Inferred basal age				60		1589–1841	1715

shed below. The regional architecture of the thrust nappe (Paulsen et al., 2020) and younger brittle faults and fractures (Indrevær et al., 2013) has clearly had a large imprint on the bedrock of Vanna, controlling how and where the bedrock destabilises at a local level. As the unstable Skredkallen mass evolved and deformed, it disintegrated along pre-existing brittle structures. Further, within the RSD area, there is a strong relationship between the brittle bedrock structure (joint sets J1–J4) and morphostructure (Fig. 10). We find a consistent alignment of morphostructures: e.g., backscarps, scarps, counterscarps and open fractures, all utilizing the mapped joint sets. These morphostructures also align well with the regional Mesozoic-age fault-fracture traces on Vannøya (Bergh et al., 2007; Davids et al., 2013; Indrevær et al., 2013), including the NE-SW trending Skipsfjord-Slettnes Fault (Fig. 8). All of these brittle structures can be ascribed to Mesozoic and Cenozoic extension and opening of the North Atlantic Ocean along the Norwegian coastal margin (Indrevær et al., 2013).

In addition, the main foliation with enclosed, partly cataclastic reworked mylonitic shear zones likely facilitates a lowered shear strength of the host rock mass in places (cf. Vick et al., 2020a). We suggest these pre-existing shear zones are utilised for sliding in the rock slope subsurface; however no shear strength values are available for the site which would shed further light on the failure mechanism. The foliation is sub-horizontal to gently-dipping, mostly obliquely down slope. It does not represent a significant weakness and therefore sliding may have been aided by the contrastingly weaker nature of the pre-existing shear zones. We also consider that the rock mass strength may be lowered due to normal fault action and fluid flow supplied to the area by the Skipsfjord-Slettnes Fault and related Mesozoic fracture/joint systems formed during a Mesozoic rifting phase (Davids et al., 2013). Minerogenic coatings on joint surfaces (Table 1) and crystal growths imply this has occurred.

While it is possible to perform a kinematic analysis to determine failure mechanism, this type of analysis is more suited to outcrop-scale case studies and tends to over-simplify large complex and three-dimensional rock slope deformations. A single failure surface is unlikely for the Skredkallen site. Conceptually, we propose a compound sliding mechanism (described by e.g. Vick et al., 2020a, 2020b), where the sliding zone or surface is made up of structures including joint set 3 (JS3) and foliation, which together have developed a step-path geometry and formed a 'failure zone' of crushed rock, mylonite or gouge in a band along their intersection (Fig. 11). The stepped shape of the rock avalanche source area indicates that a step-path failure surface is likely.

Future failure will depend on both the rock mass reaching a critical low strength state, and triggering events. Increased trigger frequency is expected in the coming century as a result of climate change in the region (Verpe Dyrrdal et al., 2020). The hazard event, and its runout distance, will be controlled by the size of failure, in turn controlled by favourable joint sets and their interaction with the mylonitic foliation in the bedrock. There are no settlements immediately below the slope, and long runout failures only pose a threat to a holiday cabin and hiking trails. Skredkallen will likely be ranked as low risk in the national RSD inventory (NGU: Geological Survey of Norway, 2021a).

5.2. Timing of postglacial events

Deglaciation of Vanna occurred between 15 and 14 cal. ka BP. At this time glacioisostatic rebound began to adjust from the removed ice load, and the ML is mapped at 47 m asl in our study area. The regional YD glacial re-advance did not reach Vanna, but the indistinct erosional notch in the landscape of the mapped area at 21–22 m asl, identified as the Main shoreline (Fig. 12b), corresponds with timing within the YD at 12.2 cal ka. BP (Andersen, 1968; Corner and Haugane, 1993). Continued uplift after the YD led to rapid land emergence, exposing marine sediments above sea level. A marine transgression, due to greater eustatic sea level rise than isostatic rebound, produced the Tapes shoreline, 12 m asl at 7.6–7.2 cal. ka BP (Corner and Haugane, 1993). The following relative sea-level fall exposed gentle terrain below the Tapes shoreline, which allowed for the accumulation of organic material forming the widespread peatlands over marine deposits that are seen today. This evolution of the area, based on both literature and observation provides a background for the discussion of the timing of failure events.

The two chronological boundaries bracketing the prehistoric rock avalanche are the retreat of glacial ice from Vanna (>14 cal. ka BP), and the age of the organic matter sampled from Pond 1 (1.7 cal. ka BP, Fig. 16, Table 2). Between these boundaries several markers attest to the history of the deposit. The notable absence of a ML shoreline on the rock avalanche deposits, which formed immediately after deglaciation and is traceable running both north and south of the lobe at 47 m asl, and erosion of the deposits along the 22 m elevation of the Main (YD) shoreline suggests avalanche activity after 15–14 cal. ka BP and prior to 12.2 cal. ka BP. This is in agreement with Norwegian case studies suggesting that the peak of Holocene rock slope failure activity occurred soon after deglaciation (e.g. Hermanns et al., 2017), due to stress release by ice unloading and isostatic rebound, as well as several of the case studies discussed in the introduction chapter (e.g. Fenton et al., 2011). However, the bounding brackets for range of ages the YD shoreline is 13.8–10.2 cal. ka BP. It is therefore somewhat unrealistic to constrain the minimum age of the failure event so tightly. The large time gap between the shorelines' formation and minimum age from the sediment dating may be explained in several ways. Pond 1 sediments do not provide a complete geochronology of the site since rock avalanche deposition, and this may be because the pond formed later, or explained by the low sediment production on the somewhat barren island. Alternatively, avalanche activity may have been episodic, with a rock avalanche occurring after the first main event and providing the topography for the lake to form.

5.3. Deposit characteristics and avalanche mobility

Collapse of the Laukvikfjellet ridge at Skredkallen caused fragmentation and an avalanching train of fragmented rock. As the train moved eastward onto the strandflat, the change in slope angle resulted in a reduction in kinetic energy and spreading of the material, into its current lobate form (Fig. 12). The elongated radial ridges in the rock avalanche deposits are extensional features formed during debris spreading, and are typical for large debris avalanches onto soft substrates (Dufresne and Davies, 2009). We have established the timing of the avalanche prior to 12.2 cal. ka BP, which means that the lower part of the lobe was emplaced in a marine environment. What is now the exposed subaerial strandflat of Vanna contained undrained marine sediments (NGU: Geological Survey of Norway, 2021b). As the large deposit moved downwards and into the sea, it would have entrained these sediments, ploughing them and mixing them with the deposit clasts to form the compact ridges of smooth rock avalanche material at the eastern and southern flanks of the lobe (Figs. 12, 14). Encountering 'deformable substrates' can inhibit avalanche motion at low slope angles, leading to bulldozing and the formation of compressional features (Belousov et al., 1999; Crosta et al., 2015; Dufresne and Davies, 2009). It can also increase mobility in some circumstances, by loading undrained sediments and causing failure of the substrate (Aaron and McDougall, 2019). The latter explanation is likely responsible for the high rock avalanche mobility at this site (after Velardi et al., 2020).

The rock avalanche mapped today likely occurred as one or a series of discrete failure events before the YD (our first age marker on the greater deposit body). The anomaly between the source area volume and resultant rock avalanche volume implies either:

1. The original rock avalanche extent and volume has been greatly diminished due to failure of underlying marine substrate and removal of material into the fjord below.
2. One or several larger events occurred prior to the deposits seen today, falling onto retreating ice and are now lost to the geological record.

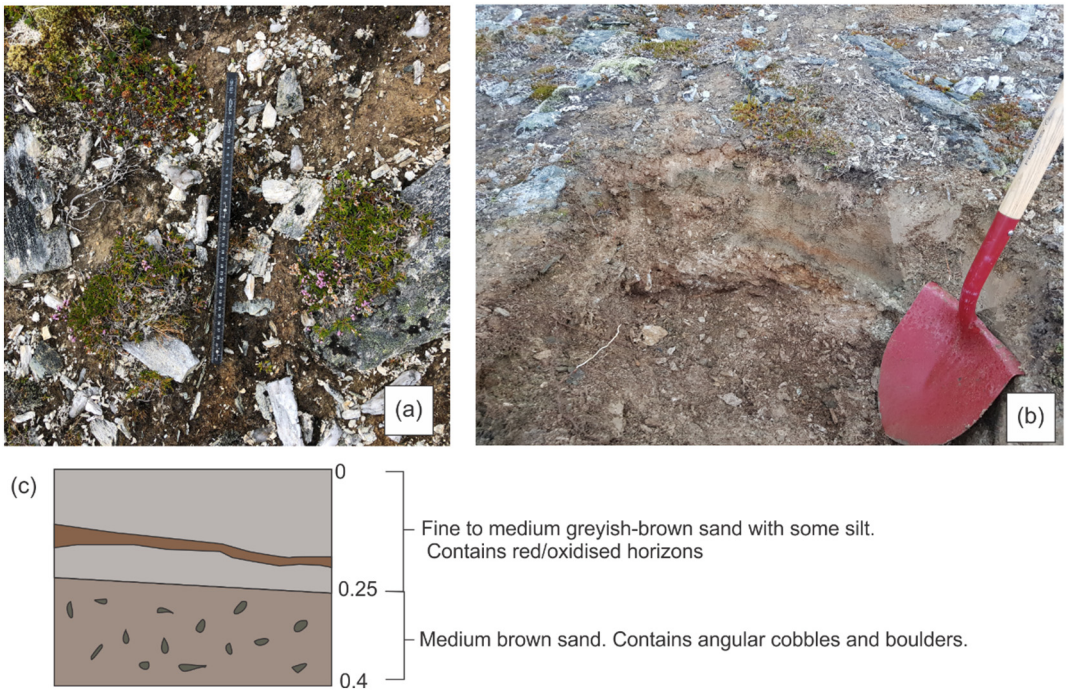

Fig. 14. (a) Smooth rock avalanche deposits at the surface, looking S. (b) A 0.4 m excavation into the smooth rock avalanche deposits. (c) Graphical log of excavation in b.

3. Weakened rock around the Skipsfjord-Slettnes fault (Fig. 6) was progressively removed due to glacial scour over a long period of time prior to deglaciation.

In any scenario, the removal of up to 32 Mm^3 of material is remarkable, and is more likely to be the result of a combination of these scenarios.

Discrete events may also have occurred between the YD and the formation of Pond 1, buried and not exposed in our geochronology window. We consider this scenario unlikely as the emplacement ridges of the deposit (Fig. 12) extend continuously from the elevation of Pond 1 to the distal portion of the lobe.

5.4. Progressive rock failure and the slope evolution at eastern Vanna

This contribution provides a window into events soon after deglaciation, and within the last 1.7 ka BP. Slope evolution in the intervening years is not resolved. We propose that the rock slope supplying the rock avalanche began to fail immediately after deglaciation, although we acknowledge that in some cases ice does not act as a sufficient buttress for rock material on the move (McColl et al., 2010), and that the failure process may have been initiated prior to deglaciation at 15–14 ka. Regardless, the progressive failure process once the slope became uncovered by ice occurred in a timeframe consistent with global reports of pre-failure endurance (>1000 years, e.g. Ballantyne, 2002; Le Roux et al., 2009). The proposed minimum age bracket for the failure event of 12.2 cal. ka BP gives a possible span of time of up to 2.8 ka for the pre-failure endurance of the slope (give the range of error with age bracket, we use this number as in indication of length of time rather than an exact measurement). During this time window temperatures were rising rapidly in northern Norway (Sjögren, 2021), resulting in an extreme adjustment period reflected by changes in e.g. slope permafrost (Lilleøren et al., 2012) and rainfall (Balascio et al., 2020). These conditions would have promoted instability (e.g. Davies et al., 2001; Eberhardt et al., 2016; Gruber et al., 2004; Krautblatter et al., 2013; Liu and Xu, 2017; Preisig et al., 2016; Hilger et al., 2020; Picarelli et al., 2016), potentially accelerating the time to failure at the site.

It is common for stress-release joints to form, propagate, and/or become enlarged in rock slopes as the newly exposed rock is unburdened and the stress-field is redistributed (McColl, 2012). The currently active RSD at Skredkallen may have begun to form as the rock mass relaxed following catastrophic failure and avalanche formation (Fig. 17b–c), with tensile stress acting on e.g., steep NW-SE striking J3 joints leading to opening of fractures along the ridge. The climatic factors which act as a catalyst for rock mass damage discussed above may have aided dislocation and deformation of the unstable mass.

It is not possible to apply the known (max. 2.8 ka) pre-failure endurance window to the current rockslide at Skredkallen determine its age (i.e. the time it began to move). Since the late-glacial/Holocene transition, the northern Norwegian climate has experienced the following climate change intervals: an early Holocene wetter period 9.5–77 cal. ka (Balascio et al., 2020), a mid-Holocene shift to a drier climate (7.8–-3.8 cal. ka BP; Balascio et al., 2020) with pronounced warming during the HTM (8.5–4.3 cal. ka BP; Huntley et al., 2013); the late Holocene marked by an increasingly cooler and wetter climate (3.8 cal. ka BP-present; Balascio et al., 2020). It is established that warming phases are marked by abrupt transitions, while the cooling phases tend to be more gradual in onset (Corrick et al., 2020). It is possible that Skredkallen began to deform in any of these intervals, although it most likely began to fail in response to the rapid transition to the HTM in mid-Holocene. Several slopes in northern Norway are known to have begun moving during this interval, under heightened hydromechanical and hydrothermal conditioning due to climate warming (e.g. Hermanns et al., 2017; Böhme et al., 2019). The timing of the rockslide initiation could be constrained by cosmogonic nuclide dating of the backscarp exposure. This would further constrain Holocene events and potentially increase our understanding of slope behaviour in response to local climate changes.

6. Conclusions

The Skredkallen case study presents an opportunity to reconstruct periglacial events at eastern Vanna, northern Norway. A 3 Mm^3 rock avalanche occurred as a result of rock slope failure of the Laukvikfjellet

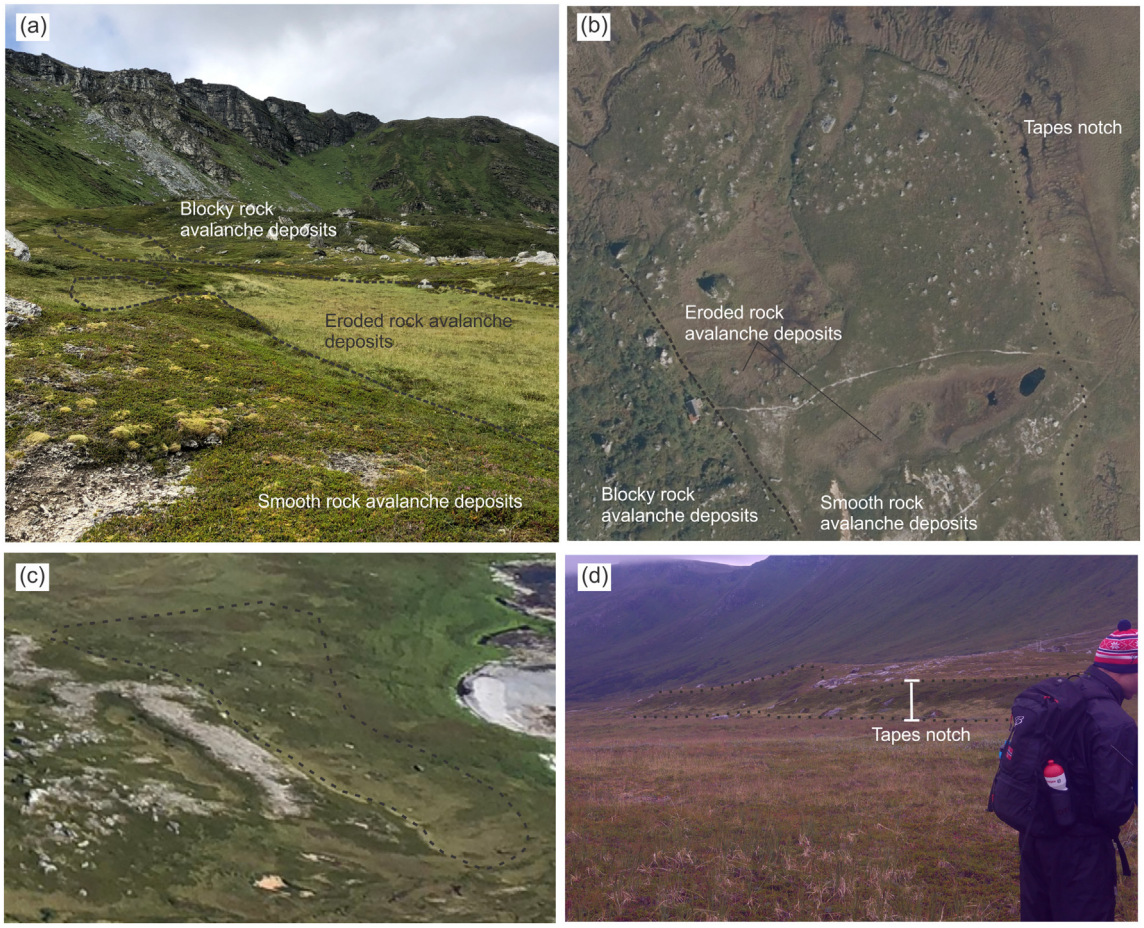

Fig. 15. Contrasting deposit morphologies. (a) Image showing an area of eroded rock avalanched deposits at the southern side of the lobe, looking NW. (b) Areal image showing north eastern side of the lobe where the boundary between smooth and blocky rock avalanche deposits is visible, as well as erosional depressions in the deposits. The Tapes notch bounds the front of the lobe here. (c) Boulders sitting in an area of eroded rock avalanche deposits- they lie outside of the Tapes notch which defines the main lobe boundary of the rock avalanche deposits. Looking NE (d) The Tapes notch in the front of the rock avalanche deposit lobe. Looking SW.

ridgeline between 15 and 12.2 cal. ka BP. The avalanche travelled >1 km from the source, and was likely transported onto soft marine sediments, which were mixed into the deposit material to form a lobe front. The release of such a large volume of avalanche material would have led to major stress relief in the remaining ridgeline, allowing the current RSD, Skredkallen, to form. The rock slope is deforming by opening along steep joints and sliding along foliation surfaces and foliation-parallel shear zones. This case study provides an insight into the mechanisms, morphology and timing of postglacial rock-slope failure events in steep, alpine terrain in northern Norway, and fills a gap in the sparse record of large failure event timings in northern Norway.

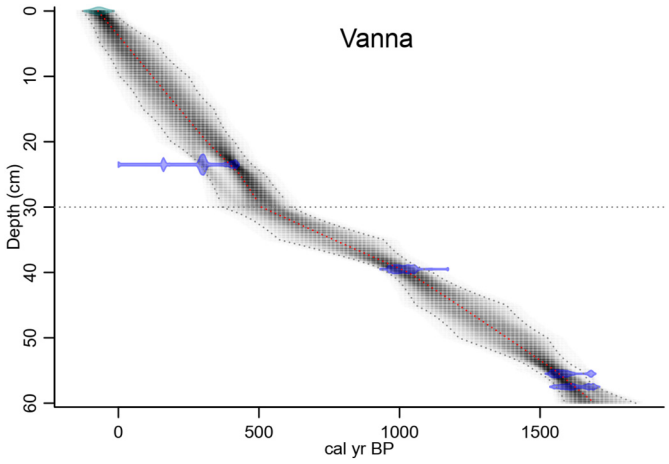

Fig. 16. Age-depth model for pond 1, Vanna, with calibrated radiocarbon ages (2σ; blue), best model based on mean ages for each depth (red dotted line) and 95% confidence intervals (grey dotted lines). Details for all radiocarbon ages are given in Table 2.

Funding

This review was conducted as part of the project 'TFK2013-012 Oppbygging av geofaglig kompetanse innen fjellskred' funded by the Troms fylkeskommune.

Declaration of competing interest

The authors declare that they have no known competing financial interests or personal relationships that could have appeared to influence the work reported in this paper.

Acknowledgements

We would like to acknowledge the 'Slettnes på Vannøya' Facebook group for reporting of prior failures at Skredkallen and other guidance. Thank you to Hanne Kristin Paulsen for first identifying this wonderful site and for field assistance. Thank you to Jean-Baptiste Kohl for ridgeline fault hunting and field assistance. Thanks to EBD for helping to overcome the maths aversion.

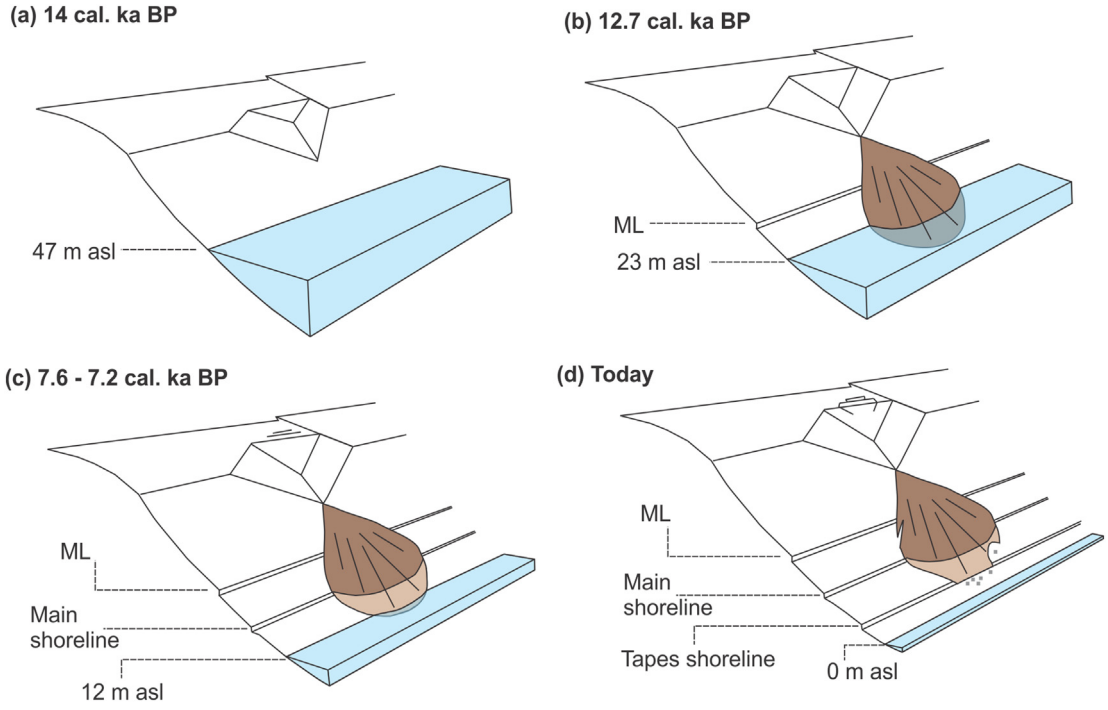

Fig. 17. Schematic timeline of the RSD and rock avalanche area site evolution at Skredkallen. Note where water elevation is indicated this is based on contemporaneous high tide level which reflects shoreline notch elevation. (a) Postglacial sea level at c. 47 m asl, with no sign of prior rock avalanche deposits. A notable amount of material is already missing from the source area. Skipsfjord-Slettnes Fault is cross-cutting the ridgeline. (b) Formation of the Main shoreline at 23 m asl. The failure has occurred, covering the ML notch. Stress release fractures have appeared above the failure, along key joint sets. (c) Tapes transgression. Shoreline is at 12 m asl (relative sea level lower prior to this). The deposits have been reworked below the Main shoreline. (d) Present day situation. The deposit has been notched at 12 m asl. Indentations in the front of the lobe represent missing sections, attributed to sliding on marine clays and wash-out of finer material. At the top of the slope, the RSD is now well-developed with lateral and back-bounding scarps displaying offset.

References

Aaron, J., McDougall, S., 2019. Rock avalanche mobility: the role of path material. Eng. Geol. 257, 105126. https://doi.org/10.1016/j.enggeo.2019.05.003.

Andersen, B.G., 1968. Glacial geology of Western Troms,North Norway. Norges Geol. Undersøkelse 256, 160.

Balascio, N.L., Anderson, R.S., D'Andrea, W.J., Wickler, S., D'Andrea, R.M., Bakke, J., 2020. Vegetation changes and plant wax biomarkers from an ombrotrophic bog define hydroclimate trends and human-environment interactions during the Holocene in northern Norway. The Holocene 30, 1849–1865. https://doi.org/10.1177/0959683620950456.

Ballantyne, C.K., 2002. Paraglacial geomorphology. Quat. Sci. Rev. 21, 1935–2017.

Ballantyne, C.K., Wilson, P.A., Gheorghiu, D., Rodés, A., 2014. Enhanced rock-slope failure following ice-sheet deglaciation: timing and causes. Earth Surf. Process. Landforms 39, 900–913.

Barboux, C., Strozzi, T., Delaloye, R., Wegmüller, U., Collet, C., 2015. Mapping slope movements in alpine environments using TerraSAR-X interferometric methods. ISPRS J. Photogramm. Remote Sens. 109, 178–192. https://doi.org/10.1016/j.isprsjprs.2015.09.010.

Belousov, A., Belousova, M., Voight, B., 1999. Multiple edifice failures, debris avalanches and associated eruptions in the Holocene history of Shiveluch volcano, Kamchatka, Russia. Bull. Volcanol. 61, 324–342. https://doi.org/10.1007/s004450050300.

Bergh, S.G., Kullerud, K., Armitage, P.E.B., Zwaan, K.B., Corfu, F., Ravna, E.J.K., Myhre, P.I., 2010. Neoarchaean to svecofennian tectono-magmatic evolution of the West Troms Basement complex, North Norway. Nor. J. Geol. 90, 21–48.

Bergh, S.G., Kullerud, K., Corfu, F., Armitage, P.E.B., Johansen, H.W., Pettersen, T., Knudsen, S., 2007. Low-grade Sedimentary Rocks on Vanna, North Norway: A New Occurrence of a Palaeoproterozoic (2.4-2.2 Ga) Cover Succession in Northern Fennoscandia, pp. 301–318.

Blikra, L.H., Christiansen, H.H., 2014. A field-based model of permafrost-controlled rockslide deformation in northern Norway. Geomorphology 208, 34–49. https://doi.org/10.1016/j.geomorph.2013.11.014.

Blikra, L.H., Longva, O., Braathen, A., Anda, E., Dehls, J.F., Stalsberg, K., 2006. Rock slope failures in Norwegian Fjord areas: examples, spatial distribution and temporal pattern. Landslides From Massive Rock Slope Fail, pp. 475–496 https://doi.org/10.1007/978-1-4020-4037-5_26.

Böhme, M., Hermanns, R.L., Gosse, J., Hilger, P., Eiken, T., Lauknes, T.R., Dehls, J.F., 2019. Comparison of monitoring data with paleo–slip rates: cosmogenic nuclide dating detects acceleration of a rockslide. Geology 47, 1–4. https://doi.org/10.1130/G45684.1/4655152/g45684.pdf.

Böhme, M., Oppikofer, T., Longva, O., Jaboyedoff, M., Hermanns, R.L., Derron, M.H., 2015. Analyses of past and present rock slope instabilities in a fjord valley: implications for hazard estimations. Geomorphology 248, 464–474. https://doi.org/10.1016/j.geomorph.2015.06.045.

Corner, G.D., Haugane, E., 1993. Marine-lacustrine stratigraphy of raised coastal basins and postglacial sea-level change at Lyngen and Vanna, Troms, northern Norway. Nor. J. Geol. 73, 175–198.

Corrick, E.C., Drysdale, R.N., Hellstrom, J.C., Capron, E., Rasmussen, S.O., Zhang, X., Fleitmann, D., Couchoud, I., Wolff, E., 2020. Synchronous timing of abrupt climate changes during the last glacial period. Science (80-.) 369, 963–969. https://doi.org/10.1126/science.aay5538.

Crosta, G., Blasio, F.V.De, Locatelli, M., Imposimato, S., Roddeman, D., 2015. Landslides falling onto a shallow erodible substrate or water layer: an experimental and numerical approach. International Symposium on Geohazards and Geomechanics (ISGG2015), p. 25 https://doi.org/10.1088/1755-1315/26/1/012004.

Davids, C., Wemmer, K., Zwingmann, H., Kohlmann, F., Jacobs, J., Bergh, S.G., 2013. K-Ar illite and apatite fission track constraints on brittle faulting and the evolution of the northern Norwegian passive margin. Tectonophysics 608, 196–211. https://doi.org/10.1016/j.tecto.2013.09.035.

Davies, M.C.R., Hamza, O., Harris, C., 2001. The effect of rise in mean annual temperature on the stability of rock slopes containing ice-filled discontinuities. Permafr. Periglac. Process. 12, 137–144. https://doi.org/10.1002/ppp.378.

Dick, G.J., Eberhardt, E., Cabrejo-liévano, A.G., Stead, D., Rose, N.D., 2013. Development of an early-warning time-of-failure analysis methodology for open-pit mine slopes utilizing ground-based slope stability radar monitoring data. Can. Geotech. J. 52, 515–529.

Dufresne, A., Davies, T.R., 2009. Longitudinal ridges in mass movement deposits. Geomorphology 105, 171–181. https://doi.org/10.1016/j.geomorph.2008.09.009.

Eberhardt, E., Preisig, G., Gischig, V., 2016. Progressive failure in deep-seated rockslides due to seasonal fluctuations in pore pressures and rock mass fatigue. Landslides Eng. Slopes. Exp. Theory Pract. 1, pp. 121–136. https://doi.org/10.1201/b21520-13.

Fenton, C.R., Hermanns, R.L., Blikra, L.H., Kubik, P.W., Bryant, C., Niedermann, S., Meixner, A., Goethals, M.M., 2011. Regional 10Be production rate calibration for the past 12ka deduced from the radiocarbon-dated Grøtlandsura and Russenes rock avalanches at 69° N,Norway. Quat. Geochronol. 6, 437–452. https://doi.org/10.1016/j.quageo.2011.04.005.

Ferretti, A., Prati, C., Rocca, F., 2001. Permanent scatterers in SAR interferometry. IEEE Trans. Geosci. Remote Sens. 39, 8–20. https://doi.org/10.1109/36.898661.

Ferretti, A., Prati, C., Rocca, F., 2000. Nonlinear subsidence rate estimation using permanent scatterers in differential SAR interferometry. IEEE Trans. Geosci. Remote Sens. 38, 2202–2212. https://doi.org/10.1109/36.868878.

Gebremedhin Nigussie, D., 2013. Numerical Modelling of Run-out of Sensitive Clay Slide Debris Daniel Gebremedhin. Norwegian Univeristy of Science and Technology.

Gisnås, K., Etzelmüller, B., Lussana, C., Hjort, J., Sannel, A.B.K., Isaksen, K., Westermann, S., Kuhry, P., Christiansen, H.H., Frampton, A., Åkerman, J., 2017. Permafrost map for Norway, Sweden and Finland. Permafr. Periglac. Process. 28, 359–378. https://doi.org/10.1002/ppp.1922.

Glastonbury, J., Fell, R., 2010. Geotechnical characteristics of large rapid rock slides. Can. Geotech. J. 47, 116–132. https://doi.org/10.1139/T09-080.
Grämiger, L.M., Gischig, V.S., 2018. Thermomechanical stresses drive damage of Alpine valley rock walls during repeat glacial cycles. J. Geophys. Res. Earth Surf., 2620–2646 https://doi.org/10.1029/2018JF004626.
Gruber, S., Hoelzle, M., Haeberli, W., 2004. Permafrost thaw and destabilization of Alpine rock walls in the hot summer of 2003. Geophys. Res. Lett. 31/L13504.
Hermanns, R.L., Blikra, L.H., Naumann, M., Nilsen, B., Panthi, K.K., Stromeyer, D., Longva, O., 2006. Examples of multiple rock-slope collapses from Köfels (Ötz valley, Austria) and western Norway. Eng. Geol. 83, 94–108. https://doi.org/10.1016/j.enggeo.2005.06.026.
Hermanns, R.L., Longva, O., 2012. Rapid rock-slope failures. In: Clague, J.J., Stead, D. (Eds.), Landslides: Types, Mechanisms And Modelling. Cambridge University Press, pp. 59–70.
Hermanns, R.L., Oppikofer, T., Anda, E., Blikra, L.H., Böhme, M., Bunkholt, H., Crosta, G.B., Dahle, H., Devoli, G., Fischer, L., Jaboyedoff, M., Loew, S., Sætre, S., Yugsi Molina, F.X., 2012. Recommended hazard and risk classification system for large unstable rock slopes in Norway. NGU Rep. 2012 (029), 49.
Hermanns, R.L., Schleier, M., Böhme, M., Blikra, L.H., Gosse, J., Ivy-ochs, S., Hilger, P., 2017. Rock-avalanche activity in W and S Norway peaks after the retreat of the Scandinavian ice sheet. In: Mikos, M., et al. (Eds.), Advancing Culture of Living With Landslides. Springer International, pp. 331–338 https://doi.org/10.1007/978-3-319-53483-1.
Hilger, P., Hermanns, R., Czekirda, J., Gosse, J., Etzelmüller, B., 2020. Permafrost as a first order control on long-term rock-slope deformation in (sub-) Arctic Norway. Quat. Sci. Rev. 251, 106718. https://doi.org/10.1016/j.quascirev.2020.106718.
Hilger, P., Hermanns, R.L., Gosse, J.C., Jacobs, B., Etzelmüller, B., Krautblatter, M., 2018. Multiple rock-slope failures from Mannen in Romsdal Valley, western Norway, revealed from Quaternary geological mapping and 10 be exposure dating. The Holocene, 095968361879816 https://doi.org/10.1177/0959683618798165.
Hungr, O., Leroueil, S., Picarelli, L., 2014. The Varnes classification of landslide types, an update. Landslides 11, 167–194. https://doi.org/10.1007/s10346-013-0436-y.
Huntley, B., Long, A.J., Allen, J.R.M., 2013. Spatio-temporal patterns in Lateglacial and Holocene vegetation and climate of Finnmark, northernmost Europe. Quat. Sci. Rev. 70, 158–175. https://doi.org/10.1016/j.quascirev.2013.03.006.
Indrevær, K., Bergh, S.G., Koehl, J.B., Hansen, J.A., Schermer, E.R., Ingebrigtsen, A., 2013. Post-Caledonian brittle fault zones on the hyperextended SW Barents Sea margin: new insights into onshore and offshore margin architecture. Nor. J. Geol. 93, 167–188.
Ivy-Ochs, S., Poschinger, A.V., Synal, H.A., Maisch, M., 2009. Surface exposure dating of the Flims landslide, Graubünden, Switzerland. Geomorphology 103, 104–112. https://doi.org/10.1016/j.geomorph.2007.10.024.
Kim, J.-H., Rimbu, N., Lorenz, S.J., Lohmann, G., Nam, S.-I., Schouten, S., Rühlemann, C., Schneider, R.R., 2004. North Pacific and North Atlantic Sea-surface temperature variability during the Holocene. Quat. Sci. Rev. 23, 2141–2154. https://doi.org/10.1016/j.quascirev.2004.08.010.
Koehl, J.B.P., Bergh, S.G., Osmundsen, P.T., Redfield, T.F., Indrevær, K., Lea, H., Bergø, E., 2019. Late Devonian–Carboniferous faulting and controlling structures and fabrics in NW Finnmark. Nor. Geol. Tidsskr. 99, 1–39. https://doi.org/10.17850/njg99-3-5.
Krautblatter, M., Funk, D., Günzel, F.K., 2013. Why permafrost rocks become unstable: a rock-ice-mechanical model in time and space. Earth Surf. Process. Landforms 38, 876–887. https://doi.org/10.1002/esp.3374.
Le Roux, O., Schwartz, S., Gamond, J.F., Jongmans, D., Bourles, D., Braucher, R., Mahaney, W., Carcaillet, J., Leanni, L., 2009. CRE dating on the head scarp of a major landslide (Séchilienne, French Alps), age constraints on Holocene kinematics. Earth Planet. Sci. Lett. 280, 236–245.
Lilleøren, K.S., Etzelmüller, B., Schuler, T.V., Gisnås, K., Humlum, O., 2012. The relative age of mountain permafrost - estimation of Holocene permafrost limits in Norway. Glob. Planet. Chang. 92–93, 209–223. https://doi.org/10.1016/j.gloplacha.2012.05.016.
Liu, X., Xu, M., 2017. The unsaturated hydromechanical coupling model of rock slope considering rainfall infiltration using DDA. Geofluids 2017. https://doi.org/10.1155/2017/1513421.
Mikkelsen, Martin, 2019. Evolution of a Rock Slope Failure at Skredkallen, Vannøya.
McColl, S., Davies, T., McSaveney, M.J., 2010. Glacier retreat and rock-slope stability: debunking debuttressing. 11th Congress of the International Association for Engineering Geology and the Environment, pp. 467–474 Auckland.
McColl, S.T., 2012. Paraglacial rock-slope stability. Geomorphology 153–154, 1–16. https://doi.org/10.1016/j.geomorph.2012.02.015.
McDougall, S., Hungr, O., 2005. Dynamic modelling of entrainment in rapid landslides. Can. Geotech. J. 42, 1437–1448.
NGU: Geological Survey of Norway, 2021a. Unstable rock slope inventory map. URL https://geo.ngu.no/kart/ustabilefjellparti_mobil/?lang=eng/ (accessed 3.19.21).
NGU: Geological Survey of Norway, 2021b. Surficial deposits national database 1:250000 (Nasjonal løsmassedatabase) [WWW Document]. URL http://geo.ngu.no/kart/losmasse/ (accessed 10.11.21).
NGU: Geological Survey of Norway, 2018. InSAR Norway. URL https://insar.ngu.no/ (accessed 9.15.19).
NMA: Norwegian Mapping Authority [Kartverkert], 2020. Height data [Norwegian: Høydedata]. Series NDH Karlsøy 2pkt 2020. URL https://hoydedata.no/LaserInnsyn/ (accessed 3.1.21).
NMA: Norwegian Mapping Authority [Kartverket], 2021a. Norwegian topographic map 4 cache [Topografisk norgeskart 4 cache]. URL https://kartkatalog.geonorge.no/metadata/topografisk-norgeskart-4-cache/8f381180-1a47-4453-bee7-9a3d64843efa.
NMA: Norwegian Mapping Authority [Statens Kartverket], 2021b. Norway in pictures [Norge i bilder]. Image date 2016-09-16, 2016-08-24, 2016-08-19, 2016-08-18, 2016-07-22. URL www.norgeibilder.no (accessed 2.18.21).
NMA: Norwegian Mapping Authority [Kartverkert], 2021;. Open water level data [Opne vasstandsdata]. URL https://www.kartverket.no/til-sjos/se-havniva (accessed 3.19.21).
MET Norway: Norwegian Meteorological Institute, 2021. seklima. URL https://seklima.met.no/observations/ (accessed 2.17.21).
Opheim, J.A., Andresen, A., 1989. Basement-cover relationships on northern Vanna, Troms,Norway. Nor. Geol. Tidsskr. 69, 67–81.
Pánek, T., 2015. Recent progress in landslide dating: a global overview. Prog. Phys. Geogr. 39, 168–198. https://doi.org/10.1177/0309133314550671.
Paulsen, H.-K., Bergh, S.G., Palinkas, S.S., 2020. Late Palaeozoic fault-controlled hydrothermal Cu–Zn mineralisation on Vanna island, West Troms Basement Complex, northern Norway. Nor. J. Geol. 1–41. https://doi.org/10.17850/njg100-1-2.
Picarelli, L., Leroueil, S., Olivares, L., Pagano, L., Tommasi, P., Urciuoli, G., 2016. Groundwater in slopes. In: Clague, J.J., Stead, D. (Eds.), Landslides: Types, Mechanisms And Modelling. Cambridge University Press, pp. 235–251.
Porter, C., Morin, P., Howat, I., Noh, M.-J., Bates, B., Peterman, K., Keesey, S., Schlenk, M., Gardiner, J., Tomko, K., Willis, M., Kelleher, C., Cloutier, M., Husby, E., Foga, S., Nakamura, H., Platson, M., Wethington Jr., M., Williamson, C., Bauer, G., Enos, J., Arnold, G., Kramer, W., Becker, P., Doshi, A., D'Souza, C., Cummens, P., Laurier, F., Bojesen, M., Foundation, N.S., 2018. ArcticDEM. https://doi.org/10.7910/DVN/OHHUKH.
Prager, C., Zangerl, C., Patzelt, G., Brandner, R., 2008. Age distribution of fossil landslides in the Tyrol (Austria) and its surrounding areas. Nat. Hazards Earth Syst. Sci. 8, 377–407. https://doi.org/10.5194/nhess-8-377-2008.
Preisig, G., 2020. Forecasting the long-term activity of deep-seated landslides via groundwater flow and slope stability modelling. Landslides 17, 1693–1702. https://doi.org/10.1007/s10346-020-01427-1.
Preisig, G., Eberhardt, E., Smithyman, M., Preh, A., Bonzanigo, L., 2016. Hydromechanical rock mass fatigue in deep-seated landslides accompanying seasonal variations in pore pressures. Rock Mech. Rock. Eng. 49, 2333–2351. https://doi.org/10.1007/s00603-016-0912-5.
Rechberger, C., Fey, C., Zangerl, C., 2021. Structural characterisation, internal deformation, and kinematics of an active deep-seated rock slide in a valley glacier retreat area. Eng. Geol. 286, 106048. https://doi.org/10.1016/j.enggeo.2021.106048.
Reimer, P.J., Austin, W.E.N., Bard, E., Bayliss, A., Blackwell, P.G., Bronk Ramsey, C., Butzin, M., Cheng, H., Edwards, R.L., Friedrich, M., Grootes, P.M., Guilderson, T.P., Hajdas, I., Heaton, T.J., Hogg, A.G., Hughen, K.A., Kromer, B., Manning, S.W., Muscheler, R., Palmer, J.G., Pearson, C., Van Der Plicht, J., Reimer, R.W., Richards, D.A., Scott, E.M., Southon, J.R., Turney, C.S.M., Wacker, L., Adolphi, F., Büntgen, U., Capano, M., Fahrni, S.M., Fogtmann-Schulz, A., Friedrich, R., Köhler, P., Kudsk, S., Miyake, F., Olsen, J., Reinig, F., Sakamoto, M., Sookdeo, A., Talamo, S., 2020. The IntCal20 Northern Hemisphere radiocarbon age calibration curve (0–55 cal kBP). Radiocarbon 62, 725–757. https://doi.org/10.1017/RDC.2020.41.
Romundset, A., Bondevik, S., Bennike, O., 2011. Postglacial uplift and relative sea level changes in Finnmark, northern Norway. Quat. Sci. Rev. 30, 2398–2421. https://doi.org/10.1016/j.quascirev.2011.06.007.
Scheidegger, A.E., 1973. On the prediction of the reach and velocity of catastrophic landslides. Rock Mech. Felsmechanik M??canique des Roches. 5, pp. 231–236. https://doi.org/10.1007/BF01301796.
Schleier, M., Hermanns, R.L., Gosse, J.C., Oppikofer, T., Rohn, J., Tønnesen, J.F., 2017a. Subaqueous rock-avalanche deposits exposed by post-glacial isostatic rebound, Innfjorddalen, Western Norway. Geomorphology 289, 117–133. https://doi.org/10.1016/j.geomorph.2016.08.024.
Schleier, M., Hermanns, R.L., Rohn, J., 2017b. Advancing culture of living with landslides. Advancing Culture of Living With Landslides https://doi.org/10.1007/978-3-319-53483-1.
Schleier, M., Hermanns, R.L., Rohn, J., Gosse, J.C., 2015. Diagnostic characteristics and paleodynamics of supraglacial rock avalanches, Innerdalen, Western Norway. Geomorphology 245, 23–39.
Schleier, Markus, Hermanns, R.L., Rohn, J., Gosse, J.C., 2015. Diagnostic characteristics and paleodynamics of supraglacial rock avalanches, Innerdalen, Western Norway. Geomorphology 245, 23–39. https://doi.org/10.1016/j.geomorph.2015.04.033.
Seequent, 2021. Leapfrog Works.
Sjögren, P.J.E., 2021. An overview of Holocene climate reconstructions in northernmost Fennoscandia. Septentrio Rep. 3, 1–31. https://doi.org/10.7557/7.5747.
Stead, D., Coggan, J.S., Elmo, D., Yan, M., 2007. Modelling brittle fracture in rock slopes - experience gained and lessons learned. In: Potvin, Y. (Ed.), Proceedings of the 2007 International Symposium on Rock Slope Stability in Open Pit Mining And Civil Engineering. Australian Centre for Geomechanics, pp. 239–252.
Stead, D., Eberhardt, E., 2013. Understanding the mechanics of large landslides. Ital. J. Eng. Geol. Environ. 85–112. https://doi.org/10.4408/IJEGE.2013-06.B-07.
Stoffel, M., Huggel, C., 2012. Effects of climate change on mass movements in mountain environments. Prog. Phys. Geogr. 36, 421–439. https://doi.org/10.1177/0309133312441010.
Stuiver, M., Reimer, P.J., Reimer, R., 2021. CALIB 8.2 [WWW program] [WWW Document]. http://calib.org.
R Core Team, 2020. R: A Language And Environment for Statistical Computing [WWW Document].
Trønnes, L., 2019. Structural Assessment And Characterisation of the Rock Slope Failure at Skredkallen, Vannøya.
Velardi, G., Hermanns, R.L., Penna, I., Böhme, M., 2020. Prediction of the reach of rock slope failures based on empirical data from Norway. ISRM Int. Symp. - EUROCK 2020.
Verpe Dyrrdal, A., Isaksen, K., Kristian Steen Jacobsen, J., Brox Nilsen, I., 2020. Present and future changes in winter climate indices relevant for access disruptions in Troms, northern Norway. Nat. Hazards Earth Syst. Sci. 20, 1847–1865. https://doi.org/10.5194/nhess-20-1847-2020.
Vick, L.M., Bergh, S.G., Höpfl, S., Percival, J., Daines, E.B., 2020a. The role of lithological weakness zones in rockslides in northern Norway. In: Li, C.C., Ødegaard, H., Høien,

A.H., Macias, J. (Eds.), ISRM International Symposium. Eurock 2020 - Hard Rock Engineering, pp. 1–9 Trondheim, Norway.
Vick, L.M., Böhme, M., Rouyet, L., Bergh, S.G., Corner, G.D., Lauknes, T.R., 2020b. Structurally controlled rock slope deformation in northern Norway. Landslides https://doi.org/10.1007/s10346-020-01421-7.
Worsley, P., 1998. Book review: rapid mass movement as a source of climatic evidence for the Holocene. The Holocene 8. https://doi.org/10.1177/095968369800800319 (372-372).
Yerro, A., Pinyol, N.M., Alonso, E.E., 2016. Internal progressive failure in deep-seated landslides. Rock Mech. Rock. Eng. 49, 2317–2332. https://doi.org/10.1007/s00603-015-0888-6.
Zerathe, S., Lebourg, T., Braucher, R., Bourlès, D., 2014. Mid-Holocene cluster of large-scale landslides revealed in the Southwestern Alps by 36Cl dating. Insight on an Alpine-scale landslide activity. Quat. Sci. Rev. 90, 106–127. https://doi.org/10.1016/j.quascirev.2014.02.015.